

HALL-EFFECT CONTROLLED GAS DYNAMICS IN PROTOPLANETARY DISKS — II: FULL 3D SIMULATIONS TOWARD THE OUTER DISK

XUE-NING BAI¹

Institute for Theory and Computation, Harvard-Smithsonian Center for Astrophysics, 60 Garden St., MS-51, Cambridge, MA 02138
Draft version March 26, 2018

ABSTRACT

We perform 3D stratified shearing-box MHD simulations on the gas dynamics of protoplanetary disks threaded by net vertical magnetic field B_{z0} . All three non-ideal MHD effects, Ohmic resistivity, the Hall effect and ambipolar diffusion are included in a self-consistent manner based on equilibrium chemistry. We focus on regions toward outer disk radii, from 5–60 AU, where Ohmic resistivity tends to become negligible, ambipolar diffusion dominates over an extended region across disk height, and the Hall effect largely controls the dynamics near the disk midplane. We find that around $R = 5$ AU, the system launches a laminar/weakly turbulent magnetocentrifugal wind when the net vertical field B_{z0} is not too weak, as expected. Moreover, the wind is able to achieve and maintain a configuration with reflection symmetry at disk midplane, as adopted in our previous work. The case with anti-aligned field polarity ($\mathbf{\Omega} \cdot \mathbf{B}_{z0} < 0$) is more susceptible to the MRI when B_{z0} drops, leading to an outflow oscillating in radial directions and very inefficient angular momentum transport. At the outer disk around and beyond $R = 30$ AU, the system shows vigorous MRI turbulence in the surface layer due to far-UV ionization, which efficiently drives disk accretion. The Hall effect affects the stability of the midplane region to the MRI, leading to strong/weak Maxwell stress for aligned/anti-aligned field polarities. Nevertheless, the midplane region is only very weakly turbulent, where the vertical rms velocity is on the order of 10^{-2} sound speed. Overall, the basic picture is analogous to the conventional layered accretion scenario applied to the outer disk. In addition, we find that the vertical magnetic flux is strongly concentrated into thin, azimuthally extended shells in most of our simulations beyond ~ 15 AU when B_{z0} is not too weak. This is a generic phenomenon *unrelated* to the Hall effect, and leads to enhanced zonal flow. Future global simulations are essential in determining the outcome of the disk outflow, magnetic flux transport, and eventually the global disk evolution.

Subject headings: accretion, accretion disks — instabilities — magnetohydrodynamics — methods: numerical — planetary systems: protoplanetary disks — turbulence

1. INTRODUCTION

The gas dynamics in protoplanetary disks (PPDs) is largely controlled by non-ideal magnetohydrodynamics (MHD) effects due to the weak level of ionization, which include Ohmic resistivity, the Hall effect and ambipolar diffusion (AD). The three effects co-exist in PPDs, with Ohmic resistivity dominating dense regions (midplane region of the inner disk), AD dominating tenuous regions (inner disk surface and the outer disk), and the Hall dominated region lies in between. While Ohmic resistivity and AD have been studied extensively in the literature, the role of the Hall effect remains poorly understood. This paper is the continuation of our exploration on the role of the Hall effect in PPDs, following Bai (2014, hereafter, paper I), where extensive summary of the literature and background information were provided in great detail.

One of the major new elements introduced by the Hall effect is that the gas dynamics depends on the polarity of the external poloidal magnetic field (\mathbf{B}_0) threading the disk. Such external field is expected to be present in PPDs as inherited from the star formation process (see McKee & Ostriker 2007 and Crutcher 2012 for an extensive review), and is also required to explain the observed

accretion rate in PPDs (Bai & Stone 2013b; Bai 2013; Simon et al. 2013b,a). Observationally, the large-scale magnetic fields have been found to thread star-forming cores (Chapman et al. 2013; Hull et al. 2014), and it is conceivable that the large-scale field with $\mathbf{B}_0 \cdot \mathbf{\Omega} > 0$ and $\mathbf{B}_0 \cdot \mathbf{\Omega} < 0$ are equally possible, where $\mathbf{\Omega}$ is along the disk rotation axis. At the scale of PPDs, particularly the scale where the Hall term is dynamically important ($\lesssim 50 - 60$ AU), one would expect different physical consequences for different field polarities.

In paper I, we focused on the inner region of PPDs ($R \lesssim 15$ AU), where the midplane region is dominated by Ohmic resistivity and the Hall effect, and the disk upper layer is dominated by AD. Without including the Hall effect, it has been found that the magnetorotational instability (MRI, Balbus & Hawley 1991) is completely suppressed in the inner disk, leading to a laminar flow and the disk launches a magnetocentrifugal wind (Bai & Stone 2013b, Bai 2013). With the inclusion of the Hall effect studied in paper I, the basic picture of laminar wind still holds, but the radial range where a laminar wind solution can be found depends on the magnetic polarity: for $\mathbf{B}_0 \cdot \mathbf{\Omega} > 0$, range of stable wind solution is expected to extend to $R \sim 10 - 15$ AU, while for $\mathbf{B}_0 \cdot \mathbf{\Omega} < 0$, the stable region is reduced to only up to $\sim 3 - 5$ AU. In addition, horizontal magnetic field is amplified/suppressed in the two cases as a result of

xbai@cfa.harvard.edu
¹ Hubble Fellow

the interplay between the Hall effect and shear (see also Kunz 2008; Lesur et al. 2014).

The studies in paper I predominantly use quasi-1D simulations to construct the laminar wind solutions. In this paper, we shift toward the outer PPDs and consider regions beyond which the MRI is expected to set in (3-15 AU depending on the strength and polarity of \mathbf{B}_0), up to the radius where the Hall effect has significant influence (~ 60 AU), and conduct full 3D simulations to accommodate turbulent fluctuations and potentially large-scale variations. In this range of disk radii, the midplane region is largely dominated by both the Hall effect and AD, and AD becomes progressively more dominated toward disk surface layer. Without including the Hall effect, it was found that the MRI is able to operate in the AD dominated midplane though the level of turbulence is strongly reduced due to AD (Bai 2013; Simon et al. 2013a). In addition, as the far-UV (FUV) ionization penetrates deeper (geometrically) into the disk, MRI operates much more efficiently in the much-better-ionized surface FUV layer (Perez-Becker & Chiang 2011; Simon et al. 2013a), which carries most of the accretion flow. The inclusion of the Hall effect is expected to modify the gas dynamics in the disk midplane region, which should also be controlled by the polarity of the large-scale magnetic field.

We begin by studying the properties of the MRI in the presence of both the Hall effect and AD using unstratified shearing-box simulations and discuss its relevance in PPDs in Section 2. In Sections 3 we describe the numerical set up for our full 3D stratified simulations of PPDs with realistic ionization profiles and run parameters. In Sections 4 and 5, we present simulation results at two focused radii, 30 AU (Section 4) and 5 AU (Section 5), emphasizing the role played by the Hall effect. We briefly discuss simulations at other disk radii (15 and 60 AU) in Section 6 which help map out the dependence of PPD gas dynamics on disk radii. We summarize the main results and discuss observational consequences, caveats and future directions in Section 7.

2. MRI WITH HALL EFFECT AND AMBIPOLAR DIFFUSION

In this section, we focus on the general properties on the non-linear evolution of the MRI in the presence of both the Hall effect and AD, applicable to the outer region of PPDs, which serve to guide more realistic simulations for the rest of this paper. All simulations are performed using the ATHENA MHD code (Stone et al. 2008), with the relevant non-ideal MHD terms implemented in our earlier works (Bai & Stone 2011, paper I). We adopt the shearing-sheet framework (Goldreich & Lynden-Bell 1965) without including vertical gravity (hence vertically unstratified). Here, dynamical equations are written in Cartesian coordinate in the corotating frame with a local disk patch with angular velocity $\Omega \mathbf{e}_z$. As a convention, (x, y, z) represent radial, azimuthal and vertical coordinates respectively. The equations are the same as Equations (2)-(5) in paper I, except the $\Omega^2 z \mathbf{e}_z$ term in the momentum equation, and the Ohmic resistivity term in the induction equation are dropped. An isothermal equation of state $P = \rho c_s^2$ is adopted with c_s being the sound speed. In code unit, we have $\rho_0 = c_s = \Omega = 1$, where ρ_0 is the initial gas den-

sity (or midplane density for stratified simulations in the following sections). The unit for magnetic field is chosen such that magnetic permeability $\mu = 1$.

In the following, we first discuss the relative importance of the Hall effect and AD in the relevant regions of PPDs. We then discuss the MRI linear dispersion relation of in the presence of both the Hall and AD terms. Finally, we proceed to non-linear unstratified shearing-box simulations. Our survey of the parameter space is by no means complete, but we have chosen the range of parameters that are most relevant to the regions of PPDs that we study in the Sections that follow (midplane regions up to ~ 60 AU).

2.1. Relative Importance of the Hall Effect and Ambipolar Diffusion in PPDs

The Hall effect is characterized by a physical scale, and in the absence of charged grains, it reads (Kunz & Lesur 2013)

$$l_H \equiv \frac{v_A}{\omega_H} = \left(\frac{\rho}{\rho_i} \right) \left(\frac{v_A}{\omega_i} \right), \quad (1)$$

where $v_A = B/\sqrt{4\pi\rho}$ is the Alfvén velocity, ω_i is the ion cyclotron frequency, $\omega_H = (\rho_i/\rho)\omega_i$ is the Hall frequency, ρ_i and ρ are the mass densities of the ions and the bulk of the gas, respectively, with $\rho_i \ll \rho$ for weakly ionized gas. Note that both v_A and ω_i are proportional to the magnetic field strength, hence l_H is field-strength independent, and is determined solely by the ionization fraction. In the disks, it is natural to normalize l_H by the disk scale height $H \equiv c_s/\Omega$. The associated Hall diffusivity η_H can be expressed as

$$\eta_H = v_A l_H. \quad (2)$$

Note that $\eta_H \propto B$.

Ambipolar diffusion is characterized by the frequency that neutrals collide with ions $\gamma_i \rho_i$, where γ_i is the coefficient of momentum transfer for ion-neutral collisions. In the disk, it is natural to normalize $\gamma_i \rho_i$ to the disk orbital frequency, by defining

$$Am \equiv \frac{\gamma_i \rho_i}{\Omega}, \quad (3)$$

which is the Elsasser number for AD. Generally, AD plays an important role in the gas dynamics when $Am \lesssim 10$ (Bai & Stone 2011). The associated AD diffusivity is given by

$$\eta_A = v_A^2 / \gamma_i \rho_i. \quad (4)$$

Note that $\eta_A \propto B^2$.

The above definitions apply when electrons and ions are the main charged species, where the physics can be described most easily. Generalizations to include charged grains can be found in, e.g., Wardle (2007) and Bai (2011a) which are used in our vertically stratified simulations in subsequent sections.

Jointly, we see that the product of the two dimensionless numbers l_H/H and Am is independent of the ionization fraction, and is given by

$$Am \cdot \left(\frac{l_H}{H} \right) = \frac{\gamma_i \rho}{\omega_i} \left(\frac{v_A}{c_s} \right) \propto \frac{\sqrt{\rho}}{c_s} \quad (5)$$

When adopting the minimum-mass solar nebula disk model (MMSN, Weidenschilling 1977; Hayashi 1981), we have that at the disk midplane, $\rho_0 \propto R^{-11/4}$, $c_s \propto R^{-1/4}$, hence $Am \cdot (l_H/H) \propto R^{-9/8}$. More specifically, we find²

$$Am \cdot \left(\frac{l_H}{H}\right) \approx 0.64 \left(\frac{R}{10\text{AU}}\right)^{-9/8}. \quad (6)$$

In the outer region of PPDs, the value of Am is found to be of order unity for a wide range of disk radii (Bai 2011a,b), and this formula provides a very useful relation in estimating the importance of AD and the Hall effect in PPDs. If we consider the Hall effect to be important when $l_H/H \gtrsim 0.1$, then the influence of the Hall effect extends to $\sim 50 - 60$ AU.

For the MRI, the relative importance of the Hall effect and AD is characterized by their respective Elsasser numbers, defined as $v_A^2/\eta\Omega$, with η being the respective diffusivities for the Hall effect (η_H) and AD (η_A). With the AD Elsasser number introduced in (3), the Hall Elsasser number can be written as (see paper I for details)

$$\chi \equiv \frac{\omega_H}{\Omega}. \quad (7)$$

Note that χ depends on field strength ($\propto B$), and also

$$\frac{l_H}{H} = \frac{1}{\chi} \frac{v_A}{c_s} = \frac{1}{\chi} \sqrt{\frac{2}{\beta}} = \frac{X}{\sqrt{2\beta}}, \quad (8)$$

where the plasma $\beta = 8\pi P/B^2$ is the ratio of gas to magnetic pressure, and $X \equiv 2/\chi$ is another commonly adopted quantity in the literature (Sano & Stone 2002a,b). The comparison between χ and Am reveal the relative importance between the Hall effect and AD, and the Hall term becomes comparably less dominant for larger χ (stronger magnetic field and smaller density). Using Equation (6), we find

$$\frac{Am}{\chi} \approx 4.5 \sqrt{\frac{\beta}{100}} \left(\frac{R}{10\text{AU}}\right)^{-9/8}. \quad (9)$$

Again, we see that Am and χ are likely of the same order for a wide range of disk radii given the typical magnetic field strength of $\beta \lesssim 100$ (saturated β) in the outer disk.

In our definition, ω_H , l_H and χ are all positive. On the other hand, the Hall effect also depends on the polarity of the magnetic field relative to Ω . To distinguish the two cases, we always state explicitly the polarity of the background magnetic field $B_{z0} > 0$ or $B_{z0} < 0$ for fields aligned and anti-aligned with Ω in this paper.

2.2. Linear Properties

The linear dispersion relation of the MRI for general axisymmetric perturbations in the Hall and AD regimes has been derived separately in Balbus & Terquem (2001) and Kunz & Balbus (2004); Desch (2004). The authors considered a general background field configuration $\mathbf{B}_0 = B_{z0}\mathbf{e}_z + B_{\phi0}\mathbf{e}_\phi$, and general axisymmetric perturbations of the form $\exp(i\mathbf{k} \cdot \mathbf{x} + \sigma t)$ with $\mathbf{k} =$

² The factor γ_i and ω_i depend on the mass of the ions. However, for the ion mass $m_i \gg m_H$, the dependence diminishes. The value computed here assumes the gas mean molecular weight $\mu = 2.33m_H$, following the formulas in Bai (2011a).

$k_x\mathbf{e}_x + k_z\mathbf{e}_z$. The main results reveal that for the MRI modes, the Hall term is coupled only to the vertical magnetic field, while the AD term is also coupled to the toroidal magnetic field. As a result, the presence of a background toroidal field has little effect on the Hall MRI, but facilitates the MRI to operate in the AD dominated regime with $Am \lesssim 1$. A joint dispersion relation including all non-ideal MHD terms was given by Pandey & Wardle (2012). It was shown that while contributions from the Hall and AD terms are independent, the joint effect is that regimes stable to pure Hall-MRI can be rendered unstable due to AD, a situation which again requires net toroidal field and strong AD ($Am \lesssim 1$).

Exploring the full parameter space of the MRI in the presence of Hall and AD effects with different field orientations with non-linear simulations is beyond the scope of this work. Here, we restrict ourselves to pure vertical background field with either $B_{z0} > 0$ or $B_{z0} < 0$. This choice makes the dispersion relation much simpler, where the most unstable mode has pure vertical wavenumber $k_z = k$, and for these modes, AD behaves the same way as Ohmic resistivity by replacing η_A with η_0 , in the linear regime. This case also covers the most essential MRI physics relevant to PPDs, since the Hall term is not directly coupled to the toroidal field, and for AD, the background toroidal field does not strongly affect the level of the MRI turbulence for $Am \gtrsim 1$ (Bai & Stone 2011).

In reference to previous works (e.g., Wardle 1999), we show in Figure 1 the MRI growth rate for pure vertical modes $k = k_z$ as a function of dimensionless wavenumber kv_{A0}/Ω and $1/\chi_0$, where subscript ‘0’ represents χ and v_A determined from background field, and similarly we use β_0 to denote plasma β for the background field. Magnetic polarity is reflected using $\text{sgn}(B_{z0})$. We consider two cases with $Am = 1$ and $Am = 100$.

For $Am = 100$ (very weak AD), the dispersion relation is well described by pure Hall MRI. For $B_{z0} > 0$, the most unstable mode always has the maximum growth rate of $0.75\Omega^{-1}$, and the most unstable wavelength λ_m shifts progressively to larger scales with $\lambda_m \propto \chi_0^{-1/2}$ as the Hall term strengthens ($\chi_0 \rightarrow 0$). Normalizing to the disk scale height, we find

$$\frac{\lambda_m}{H} \approx 4\pi \sqrt{\frac{l_H}{3H}} \left(\frac{2}{\beta_0}\right)^{1/4} \approx 0.5 \sqrt{\frac{3l_H}{H}} \left(\frac{10^4}{\beta_0}\right)^{1/4}. \quad (10)$$

For $B_{z0} < 0$, unstable modes exist only when $(1/\chi_0) < 2$, and unstable wavenumber can extend virtually to infinity when $(1/\chi_0) > 1/2$.

For $Am = 1$, we see that small-scale modes are strongly suppressed. For $B_{z0} < 0$, the most unstable modes have wave numbers of $kv_A/\Omega \sim 0.5$. In the absence of the Hall effect ($1/\chi_0 = 0$), λ_m is increased by a factor of ~ 2 due AD. For $B_{z0} > 0$ and toward stronger Hall term ($1/\chi_0 \gtrsim 5$), λ_m is less affected by AD since it is shifted to larger scales, and the maximum growth rate is only slightly reduced.

2.3. Unstratified Shearing-box Simulations

Our unstratified shearing-box simulations mainly serve for calibrating and interpreting stratified simulation results. Therefore, we do not aim at a thorough parameter study, but mainly focus on parameter regimes relevant

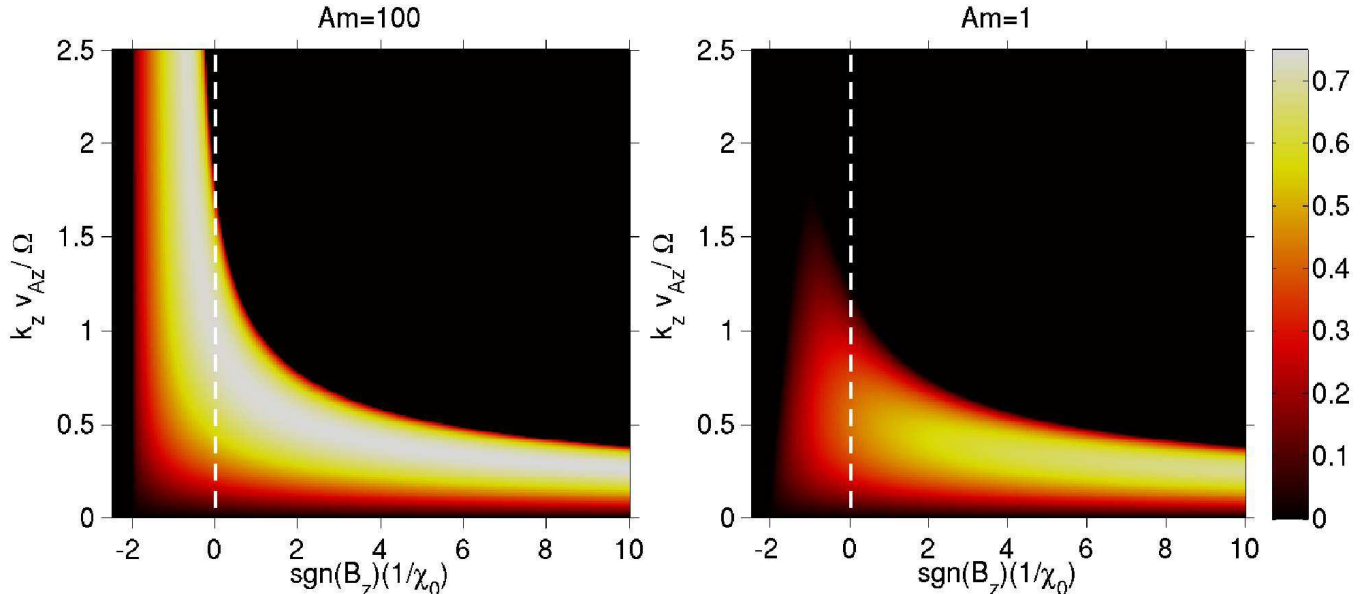


FIG. 1.— Linear growth rate of the MRI in the presence of the Hall effect and AD, in the case of pure vertical background magnetic field, and for modes with pure vertical wavenumbers $k_z = k$. Growth rate is drawn as a function of normalized wavenumber kv_A/Ω and $\text{sgn}(B_z)(1/\chi_0)$, with two panels showing results for fixed $Am = 100$ (ideal MHD) and $Am = 1$ (strong AD). Note that no unstable mode exists for $\text{sgn}(B_z)(1/\chi_0) \leq -2$.

to real PPDs. In this regard, we consider the following set of parameters:

- The Hall length $l_H = 0.1H$ or $0.3H$.
- Net vertical field strength, with $\beta_0 = 10^4$ and 10^5 .
- Magnetic field polarity, $B_{z0} > 0$ or $B_{z0} < 0$.
- The value of $Am = 1$, occasionally 10 and 100.

Our simulations use fixed box size of $4H \times 4H \times 2H$ in (x, y, z) dimensions. Note that our simulation box height is $2H$ rather than H typically used in unstratified shearing-box simulations, which has the potential to accommodate larger spatial structures while not being unrealistically tall for real disks. Our unstratified simulations can be performed with relatively high spatial resolution, 48 cells per H in the $x - z$ plane (24 in the y dimension). We can not afford the same resolution for our stratified runs in Sections 3-5, therefore, we also conduct simulations with half the resolution to justify the use of lower resolution in our stratified simulations.

We have chosen the value of $Am = 1$ appropriate for the midplane region of the outer disk. From Equation (6), the Hall length of $l_H \sim 0.1$ to $0.3H$ applies to the range of $R \sim 20$ to 50 AU. Given $\beta_0 = 10^4$ and 10^5 , the corresponding value of χ_0 ranges from 0.015 to 0.14.

For $B_{z0} < 0$, and for this range of χ_0 there is no linearly unstable MRI mode. However, this does not necessarily relate to the non-linear sustainability, given the relatively small value of l_H . Therefore, in our simulations, we first run the simulations in the ideal MHD limit to time $t = 60\Omega^{-1}$, then turn on non-ideal MHD terms and evolve further to time $t = 300\Omega^{-1}$. In Figure 2 we show the time evolution of two runs in the case of $B_{z0} < 0$, with fixed $l_H = 0.1$, $\beta_0 = 10^4$ but different $Am = 1, 10$ and 100. We see that for $Am = 100$, MRI turbulence can be

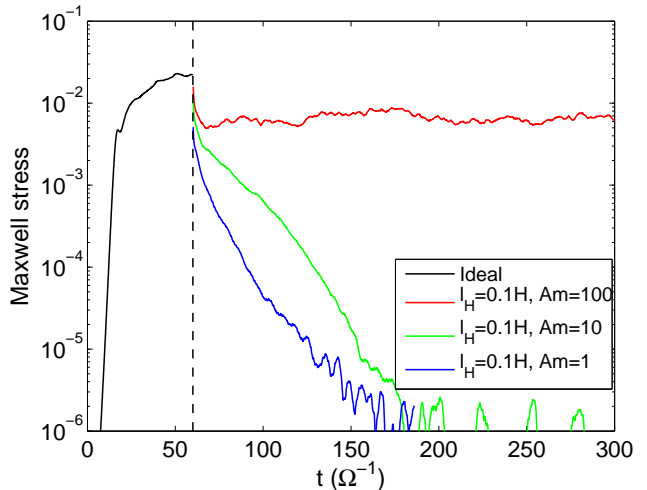


FIG. 2.— Non-linear sustainability of the MRI turbulence in the case of $B_{z0} < 0$. The run is initialized with ideal MHD with $\beta_0 = 10^4$ till $t = 60\Omega^{-1}$ before the Hall (with $l_H = 0.1H$) and AD terms are turned on. Without linearly unstable MRI mode, turbulence is sustained for $Am = 100$ but decays for $Am = 10$ and 1.

sustained but at a lower level, while for $Am = 10$ and 1, turbulence is suppressed. We have tested with other values of β_0 and l_H , and find that as long as $Am = 1$, no sustained MRI turbulence is possible. This implies that under this configuration, the midplane region of the outer disk is likely the exact analog of the conventional “dead zone”.

For $B_{z0} > 0$, the background field configuration is unstable to the MRI. We provide the list of runs and diagnostic quantities in Table 1. The runs are named in the form of $QxAyBz-Rw$, where $x = 10l_H/H$, $y = Am$, $z = \log_{10}(\beta_0)$, and w is the numerical resolution (24 or 48 per H). In all cases, we have fixed the value of

TABLE 1
LIST OF UNSTRATIFIED SIMULATION RUNS WITH $B_{z0} > 0$.

Run	Res.	Am	l_H	β_0	χ_0	E_k	E_M	α_{Rey}	α_{Max}	α	α_{mag}
Q3A1B4-R24	24	1	0.3	10^4	0.047	4.6×10^{-2}	2.4×10^{-3}	3.0×10^{-4}	5.0×10^{-4}	8.0×10^{-4}	0.21
Q3A1B4-R48	48	1	0.3	10^4	0.047	3.1×10^{-2}	3.6×10^{-3}	3.8×10^{-4}	7.8×10^{-4}	1.2×10^{-3}	0.22
Q3A1B5-R24	24	1	0.3	10^5	0.015	1.4×10^{-2}	3.7×10^{-3}	4.3×10^{-4}	8.8×10^{-4}	1.3×10^{-3}	0.24
Q3A1B5-R48	48	1	0.3	10^5	0.015	1.4×10^{-2}	4.2×10^{-3}	5.1×10^{-4}	9.8×10^{-4}	1.5×10^{-3}	0.23
Q1A1B4-R24	24	1	0.1	10^4	0.14	1.6×10^{-2}	2.6×10^{-3}	5.9×10^{-4}	6.1×10^{-4}	1.2×10^{-3}	0.24
Q1A1B4-R48	48	1	0.1	10^4	0.14	1.7×10^{-2}	4.9×10^{-3}	9.3×10^{-4}	1.2×10^{-3}	2.1×10^{-3}	0.25
Q1A1B5-R24	24	1	0.1	10^5	0.045	1.0×10^{-2}	1.7×10^{-3}	3.8×10^{-4}	2.3×10^{-4}	6.1×10^{-4}	0.14
Q1A1B5-R48	48	1	0.1	10^5	0.045	9.8×10^{-3}	1.1×10^{-3}	3.9×10^{-4}	2.3×10^{-4}	6.1×10^{-4}	0.20

l_H is normalized to H , E_k and E_M are normalized to midplane gas pressure $\rho_0 c_s^2$. See Section 2.3 for details.

$Am = 1$. We find that vigorous turbulence is quickly developed for all runs. Many of these runs show secular effects in their evolution (to be discussed later), hence we run these simulations for very long time to $t = 1440\Omega^{-1}$ and extract turbulence statistics by performing time and volume averages after $t = 1120\Omega^{-1}$ (denoted by the over line). Major diagnostic quantities include the kinetic energy density $E_k = \overline{\rho v^2/2}$, magnetic energy density $E_M = \overline{B^2/2}$, the Maxwell stress $\alpha^{\text{Max}} \equiv -\overline{B_x B_y}$ and Reynolds stress $\alpha^{\text{Rey}} \equiv \overline{\rho v_x v_y}$ (normalization $\rho_0 c_s^2$ is omitted since it equals 1 in code unit). The total Shakura-Sunyaev α is $\alpha^{\text{Max}} + \alpha^{\text{Rey}}$. Another useful diagnostic is $\alpha^{\text{mag}} \equiv \alpha^{\text{Max}}/E_M$ (e.g. Hawley et al. 2011; Sorathia et al. 2012), which is considered as a useful indicator for numerical convergence.

First, we find that for relatively large $l_H = 0.3H$, and relatively strong field $\beta_0 = 10^4$, strong zonal field (Kunz & Lesur 2013) is gradually built up on relatively long timescales (~ 100 orbits), which results from concentration of vertical magnetic flux pertaining to the Hall effect. In Figure 3, we show the final snapshot of our run Q3A1B4-R48 at time $t = 1440\Omega^{-1}$, which clearly shows the zonal field structure. On the other hand, we find that the zonal field coexists with vigorous turbulence, and gives an α value of $\sim 10^{-3}$. The presence of vigorous turbulence, rather than remaining in the “low-transport state”, is largely due to relatively strong magnetic diffusion with $Am = 1$, which acts against the buildup of magnetic flux as discussed in Kunz & Lesur (2013). We do not observe such prominent zonal field structures in other runs with smaller l_H and weaker magnetic fields.

In the mean time, we find that in essentially all of our unstratified simulations, density variation also show significant zonal structure, leading to strong zonal flows to balance the pressure gradient of the zonal density variation (Johansen et al. 2009). Such density variation is not captured in Kunz & Lesur (2013) due to their usage of incompressible code. The density variation for our run Q3A1B4-R48 is shown in the bottom panel of Figure 3, which exhibits excessive density variation of $\sim 50\%$. As a result, the kinetic energy displayed in Table 1 is largely dominated by the kinetic energy associated with the zonal flow ($v_y \sim 0.2 - 0.3c_s$). Other runs develop weaker zonal density variations, and weaker zonal flows as well, which take place over more than 100 orbital timescale and show secular variations. Full discussion on such zonal flows is beyond the scope of this paper, but

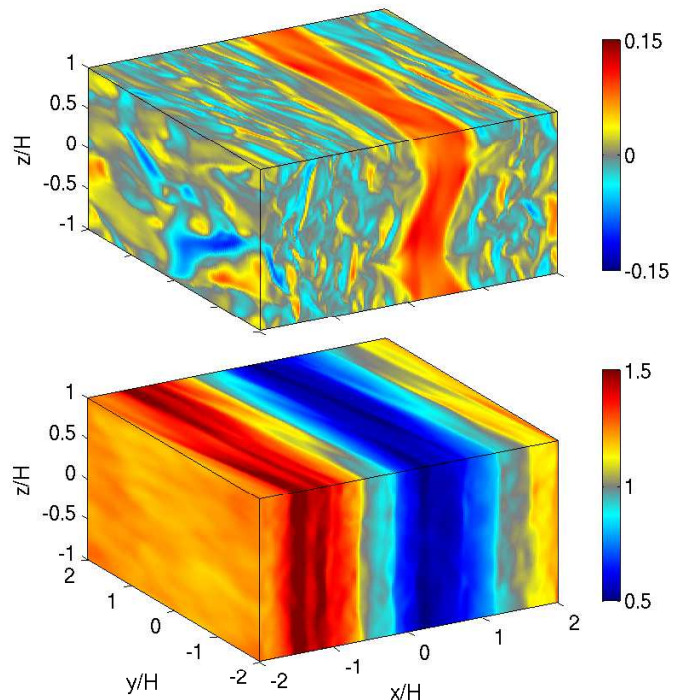


FIG. 3.— Snapshot from the end of our unstratified run Q3A1b4-R48 with $Am = 1$, $l_H = 0.3H$ and $B_{z0} > 0$. The top panel shows the vertical magnetic field B_{z0} , and the bottom panel shows the gas density ρ .

phenomenologically, we observe that stronger zonal flow is launched for larger l_H and stronger background field from our unstratified simulations.

In all our simulations, sustained MRI turbulence at the level of $\alpha \sim 10^{-3}$ is obtained. Stronger background vertical field leads to stronger turbulence, and larger l_H also leads to stronger turbulence until the zonal field configuration is developed, where turbulence level is reduced. We caution that for the parameters considered here, the most unstable MRI mode is not well resolved. For best resolved case (run Q3A1B4-R48), we find from Equation (10) that the most unstable wavelength amounts to about 13 cells. We do not expect our simulations to show unambiguous convergence on the value of α (and in fact the value of α is also affected by the development of the zonal flows, which show long timescale variations). Nevertheless, by looking at the value of α_{mag} , we find that the low

and high resolution simulations give consistent values for all cases except for run Q1A1B5. Moreover, by inspecting the snapshots in runs with different resolutions, we find their evolutionary behaviors are qualitatively similar in all cases. This gives us confidence that 24 cells per H adopted in our stratified runs is sufficient to capture the of essential properties of the MRI in the Hall-AD regime.

In sum, our unstratified simulations of the MRI in the presence of both the Hall effect and AD indicate that under conditions appropriate for the outer region of PPDs ($Am \sim 1$), MRI can not be self-sustained in the midplane if $B_{z0} < 0$, while for $B_{z0} > 0$, the self-sustained turbulence always exists at the level of $\alpha \sim 10^{-3}$. We find zonal fields when the Hall term and background field is relatively strong, and find zonal flows develop in all cases.

3. SETUP OF 3D STRATIFIED SIMULATIONS

We perform a series of 3D stratified shearing-box simulations where all non-ideal MHD effects are included self-consistently. The set up of the simulations follow closely to those in paper I, with formulation given in his Section 2.1-2.2 and methodology given in Section 3.1. In brief, we consider a MMSN disk. At a given radial location R , we produce a diffusivity table based on equilibrium chemistry using the chemical reaction network developed in our earlier works (Bai & Goodman 2009; Bai 2011a) and the latest version of the UMIST database (McElroy et al. 2013). Dust grains of $0.1\mu\text{m}$ in size and abundance of 10^{-4} is assumed³. Standard sources of ionization including cosmic rays, X-rays and radioactive decay are included. We further include an effective treatment of the far-UV (FUV) ionization which substantially reduces non-ideal MHD effects toward disk surface, calibrated with the models of Walsh et al. (2010, 2012). The gas essentially behaves in the ideal MHD regime in the FUV ionization layer. The diffusivities have the form $\eta_O, \eta_H \propto B$ and $\eta_A \propto B^2$, which is applicable given the small grain abundance.

Unlike in paper I, simulations in this work are full-3D, since we expect the development of MRI turbulence. All our simulations have vertical domain extending from $z = -6H$ to $6H$ using a resolution of 24 cells per H in x and z , and half the resolution in y . A density floor of $5 \times 10^{-6}\rho_0$ is applied for all simulations to avoid numerical difficulties in the strongly magnetized disk surface region (where $\rho_0 = 1$ is the midplane gas density in code unit). For simulations in Section 4 (at $R = 30$ AU), we use very extended horizontal box size of $6H \times 12H$ in (x, y) to better accommodate potentially large-scale structures. Note that for MMSN disk at 30 AU, the disk aspect ratio $H/R \approx 0.078$, hence the radial box size ~ 14 AU, which is about the maximum size where shearing-sheet approximation can be considered as reasonable. Smaller horizontal domain size of $4H \times 8H$ is used for simulations

³ We find that using the complex chemical reaction network, the resulting ionization fraction in low density and low temperature regions is, surprisingly, higher than the grain-free case (the same does not hold when considering the simple network of Oppenheimer & Dalgarno (1974)). Since this occurs mainly in the FUV-dominated surface layer of the outer disk ($\gtrsim 30$ AU) where the gas behaves in the ideal MHD regime, our simulation results are insensitive to this fact. For consistency we also produce a diffusivity table with grain-free chemistry and choose the one with higher diffusivity in the final table.

in Sections 5-6 to reduce computational cost.

All simulations are started with all non-ideal MHD terms turned on, and are initialized with uniform vertical magnetic field B_{z0} characterized by midplane plasma β_0 , together with a sinusoidally varying (in x) vertical field B_{z1} to avoid strong initial channel flows (Bai & Stone 2013a). To allow the simulations to saturate quickly, we choose the amplitude of B_{z1} to be four times B_{z0} , and four wavelength of the sinusoidal variations in x :

$$B_z = B_{z0} + 4B_{z0} \sin\left(\frac{4 \times 2\pi x}{L_x}\right) \quad (11)$$

Simulations are typically run for about 153 orbits to $t = 960\Omega^{-1}$ or about 115 orbits to $t = 720\Omega^{-1}$.

We have slightly modified the vertical outflow boundary condition compared with paper I. Here, the boundary condition assumes hydrostatic equilibrium in ρ , outflow in v_z , zero gradient in B_z , v_x and v_y (same as paper I), while B_x and B_y are reduced proportionally as density in the ghost zones (different from paper I, same as in Simon et al. 2013a). We do observe that the evolution of mean magnetic fields somewhat depends on the treatment of the outflow boundary condition, which reflects the limitation of shearing box when using open boundaries in the presence of disk outflow. Some of its influences will be discussed in the main text. Nevertheless, the general properties of the flow do not sensitively depend on the choice of vertical boundary condition (Fromang et al. 2013).

We consider disk radii of $R = 5$ AU, 15 AU, 30 AU and 60 AU, where at each radius we consider $\beta_0 = 10^4$ and 10^5 , and for both magnetic polarities. We mainly focus on two disk radii: $R = 30$ AU (Section 4), where we further conduct Hall-free simulations for detailed comparison; and $R = 5$ AU (Section 5), where comparisons with quasi-1D simulations in paper I will be made. All 3D simulations are listed in Table 2, and each run is named as $Rxb yH*$, where x represents disk radius in AU, $y = \log_{10}\beta_0$, and $*$ can be 0, ‘+’ or ‘-’ for simulations excluding the Hall term (0), with the Hall term and $B_{z0} > 0$, with the Hall term and $B_{z0} < 0$.

4. SIMULATION RESULTS: 30 AU

We focus on $R = 30$ AU in this section. We choose this radius because we find that at this location, the Hall effect around disk midplane is about equally important as AD. The disk is likely to develop more stable configurations at smaller disk radii (for $B_{z0} > 0$) as found in paper I, while the Hall effect becomes less prominent toward larger radii. This location has been explored in Simon et al. (2013b,a), where only AD was taken into account with fixed profile of $Am = 1$ near the midplane. Our new simulations self-consistently take into account the ionization-recombination chemistry, together with the inclusion of the Hall effect.

We perform a total of 6 simulations with $\beta_0 = 10^5$ and 10^4 . All these runs lead to vigorous MRI turbulence in the surface layer, and in the presence of net vertical magnetic field, they always launch outflows. Different aspects of these simulations are discussed in the subsections below.

4.1. Evolution of Large-scale Toroidal Field

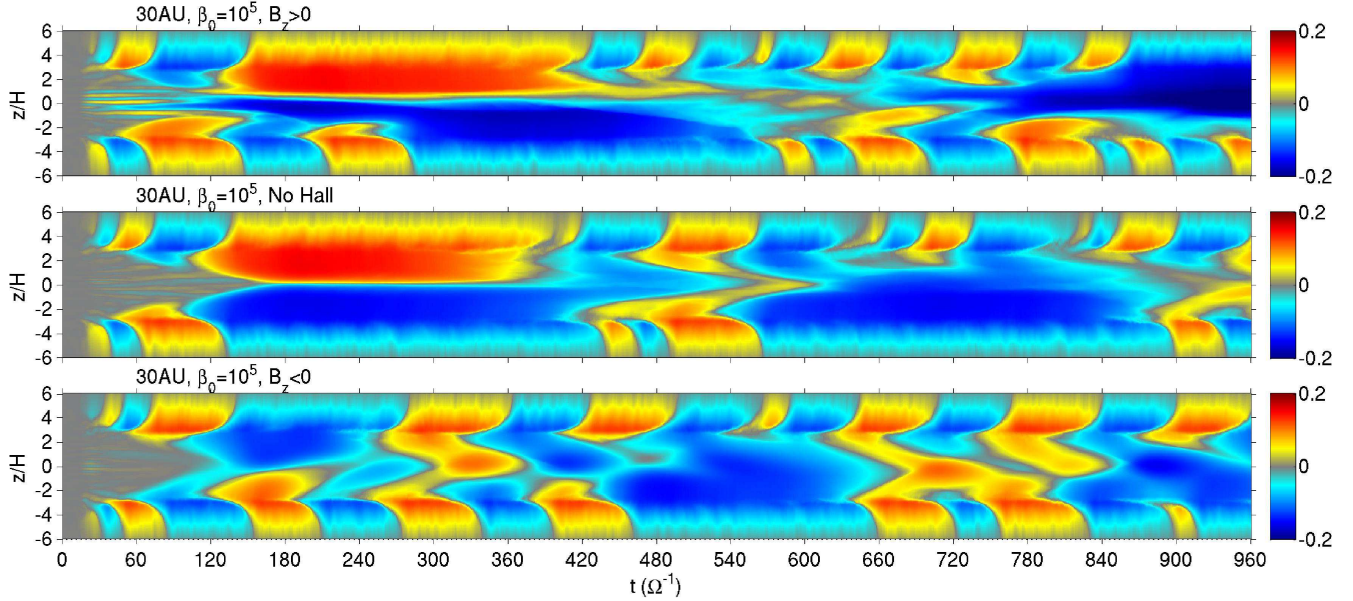


FIG. 4.— The time evolution for the vertical profile of horizontally averaged B_y in our runs at 30 AU with $\beta_0 = 10^5$. The top, middle and bottom panels correspond to runs R30b5H+, R30b5H0 and R30b5H–, i.e., Hall turned on with $B_{z0} > 0$, Hall-free, and Hall turned on with $B_{z0} < 0$.

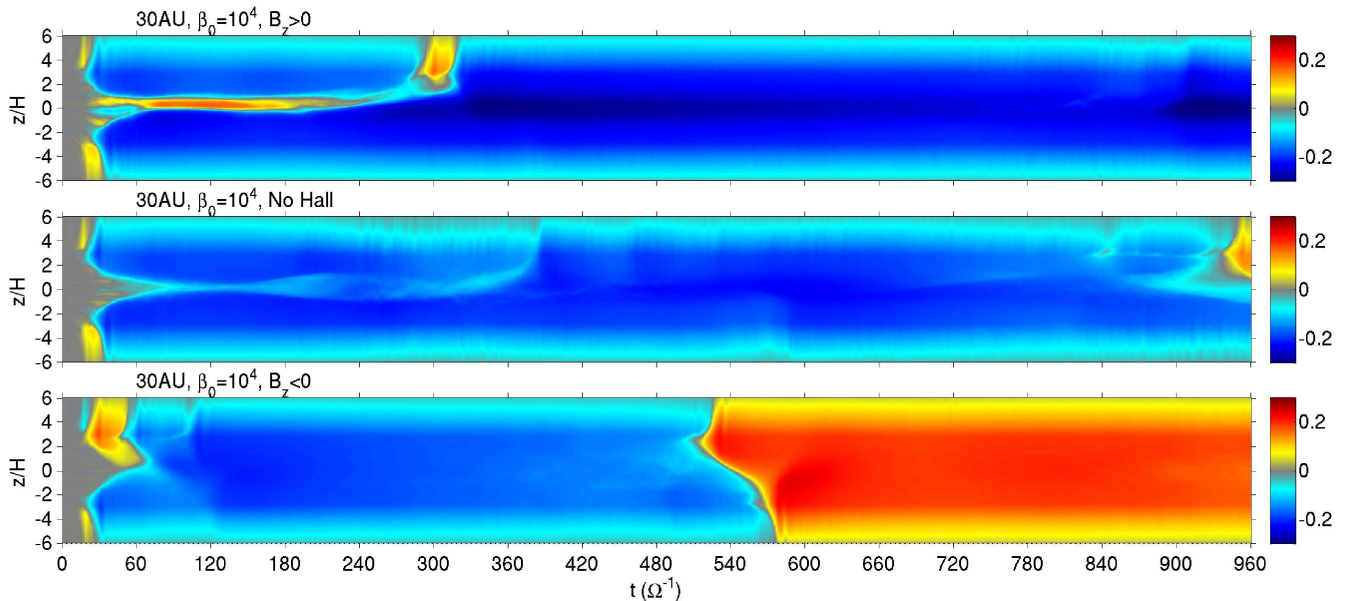


FIG. 5.— Same as Figure 4, but for runs at 30 AU with $\beta_0 = 10^4$.

Global evolution of the system is largely controlled by magnetic fields, hence we first discuss the overall evolution of large-scale toroidal field from our simulations as a standard diagnostic. Starting from runs with $\beta_0 = 10^5$: R30b5H+, R30b5H0 and R30b5H–, we show in Figure 4 the time evolution of horizontally averaged B_y for all three runs. Since the initial conditions for these simulations are identical (except for negative sign of B_{z0} for run R30b5H–), these runs initially proceed in a similar way. The Hall and AD terms become progressively more important as (midplane) magnetic fields become stronger and the three runs then evolve differently. All three cases show prominent level of dynamo activities emanating from the surface layer, where the sign of mean

B_y alternates over time. The alternation behavior is quite irregular, and to some extent similar to ideal MHD simulations with modestly strong vertical magnetic flux ($\beta_0 \gtrsim 10^3$, Bai & Stone 2013a), which contrasts with the conventional MRI dynamo (zero net vertical magnetic field in ideal MHD) with very periodic cycles of about 10 orbits (e.g., Davis et al. 2010; Shi et al. 2010).

We next discuss simulations with $\beta_0 = 10^4$, with three runs R30b4H+, R30b4H0 and R30b4H–. Similar to the weaker field case, all three runs develop vigorous turbulence mainly in the surface layer due to FUV ionization (see next subsection). The time evolution of horizontally averaged B_y for the three runs is shown in Figure 5. We see that the MRI dynamo is suppressed in

TABLE 2
LIST OF STRATIFIED SIMULATION RUNS.

Run	R (AU)	Hall?	B_{z0}	β_0	Box size (H)	T (Ω^{-1})	α^{Max}	α^{Rey}	δv_z	M_{out}	$ T_{z\phi}^{\text{Max}} $	Section
R5b5H+	5	Yes	+	10^5	$4 \times 8 \times 12$	360	6.5×10^{-3}	1.6×10^{-5}	1.0×10^{-2}	3.0×10^{-4}	3.1×10^{-4}	5
R5b5H-	5	Yes	-	10^5	$4 \times 8 \times 12$	360	4.2×10^{-4}	3.4×10^{-5}	5.0×10^{-3}	1.1×10^{-4}	1.64×10^{-4}	5
R5b4H-	5	Yes	-	10^4	$4 \times 8 \times 12$	360	1.3×10^{-3}	4.6×10^{-4}	1.4×10^{-3}	3.2×10^{-4}	6.7×10^{-4}	5
R15b5H+	15	Yes	+	10^5	$4 \times 8 \times 12$	720	2.3×10^{-3}	1.3×10^{-4}	5.2×10^{-3}	2.9×10^{-4}	2.5×10^{-4}	6.1
R15b5H-	15	Yes	-	10^5	$4 \times 8 \times 12$	720	7.2×10^{-4}	2.8×10^{-5}	2.4×10^{-3}	2.3×10^{-4}	2.4×10^{-4}	6.1
R15b4H+	15	Yes	+	10^4	$4 \times 8 \times 12$	720	2.3×10^{-3}	3.1×10^{-4}	8.2×10^{-3}	6.1×10^{-4}	8.8×10^{-4}	6.1
R15b4H-	15	Yes	-	10^4	$4 \times 8 \times 12$	720	3.0×10^{-3}	1.7×10^{-4}	8.6×10^{-3}	8.0×10^{-4}	1.1×10^{-3}	6.1
R30b5H+	30	Yes	+	10^5	$6 \times 12 \times 12$	960	1.9×10^{-3}	3.9×10^{-4}	2.0×10^{-2}	2.2×10^{-4}	2.1×10^{-4}	4
R30b5H0	30	No	+	10^5	$6 \times 12 \times 12$	960	1.5×10^{-3}	2.9×10^{-4}	1.5×10^{-2}	2.3×10^{-4}	2.2×10^{-4}	4
R30b5H-	30	Yes	-	10^5	$6 \times 12 \times 12$	960	1.4×10^{-3}	2.2×10^{-4}	1.3×10^{-2}	2.3×10^{-4}	2.2×10^{-4}	4
R30b4H+	30	Yes	+	10^4	$6 \times 12 \times 12$	960	6.1×10^{-3}	4.4×10^{-4}	2.0×10^{-2}	1.5×10^{-3}	1.7×10^{-3}	4
R30b4H0	30	No	+	10^4	$6 \times 12 \times 12$	960	4.8×10^{-3}	5.4×10^{-4}	2.4×10^{-2}	1.1×10^{-3}	1.4×10^{-3}	4
R30b4H-	30	Yes	-	10^4	$6 \times 12 \times 12$	960	5.0×10^{-3}	6.5×10^{-4}	2.4×10^{-2}	1.2×10^{-3}	1.4×10^{-3}	4
R60b5H+	60	Yes	+	10^5	$4 \times 8 \times 12$	720	2.9×10^{-3}	5.7×10^{-4}	2.5×10^{-2}	2.4×10^{-4}	2.2×10^{-4}	6.2
R60b5H-	60	Yes	-	10^5	$4 \times 8 \times 12$	720	2.6×10^{-3}	5.0×10^{-4}	2.1×10^{-2}	2.4×10^{-4}	2.1×10^{-4}	6.2
R60b4H+	60	Yes	+	10^4	$4 \times 8 \times 12$	720	9.3×10^{-3}	4.4×10^{-4}	8.9×10^{-3}	2.0×10^{-3}	1.9×10^{-3}	6.2
R60b4H-	60	Yes	-	10^4	$4 \times 8 \times 12$	720	7.3×10^{-3}	4.3×10^{-4}	1.1×10^{-2}	1.8×10^{-3}	2.0×10^{-3}	6.2

Note: α^{Max} and α^{Rey} are computed within $z = \pm 4.5H$, $T_{z\phi}^{\text{Max}}$ is evaluated at $z = \pm 4.5H$, and δv_z is the turbulent vertical velocity within $z = \pm 2H$. See Section 4 for details.

all cases and the mean toroidal field is predominantly one sign. This is generally a consequence of stronger net vertical field, which is an analog of the ideal MHD case (Bai & Stone 2013a). While the system is turbulent, toroidal field is always the dominant field component, and when the dynamo is suppressed, this field component is dominated by the mean field. Therefore, the space-time plot of mean B_y largely characterizes the evolution of the system. However, by viewing individual simulation snapshots, localized patches possessing opposite sign of toroidal field do exist in runs R30b4H0 and R30b4H-. In the latter case, the region with opposite B_y gradually grows and eventually leads to the reversal of mean toroidal field in the disk (bottom panel of the Figure). We have continued this run further and found that the mean B_y will reverse again after another ~ 50 orbits, and this cycle is likely to continue. Similarly, positive B_y region started to dominate the upper half of the disk near the end of our run R30b4H0.

The secular evolution of the mean field discussed above exists in all our simulations to a certain extent, which is partly related to the limitations of the shearing-box approach: due to the imposed net vertical field which presumably connects to infinity, the mean field in the disk should be in causal contact with the field beyond, but the causal connection is truncated with prescribed outflow boundary condition. Since most activities in the disks are magnetically-driven, the secular evolution of the mean fields also makes the level of turbulence in the disks time variable. For example, in run R30b4H-, the midplane region exhibits stronger turbulent activities around time $t = 480 - 600\Omega^{-1}$ with turbulent velocity about a factor of 3 higher than some other periods. Therefore, the readers should bear in mind about the potential uncertainties due to such variabilities. To obtain the vertical profiles of various diagnostic quantities in the next subsection, we will perform time average for around 75–100

orbits, expecting relatively long-term averages to provide reasonably realistic mean values.

4.2. Stress Profiles and Level of Turbulence

Based on the time evolution of the mean field, we extract useful diagnostic quantities and average them in time from $t = 480\Omega^{-1}$ onward for simulations with $\beta_0 = 10^5$, and from $t = 360\Omega^{-1}$ onward for simulations with $\beta_0 = 10^4$. In Figures 6 and 7, we show the time-averaged vertical profiles of various diagnostic quantities from these simulations.

The relative importance of various non-ideal MHD effects can be best viewed from the top left panel of Figure 6 and the left panel of Figure 7, which show the profiles of the Elsasser numbers (based on the Hall-free run in each case, but the runs with Hall term generally give almost the same profiles). Clearly, Ohmic resistivity is completely negligible with $\Lambda \gg 100$ at all heights. With $\beta_0 = 10^5$, both the Hall effect and AD are important within $z \sim \pm 2 - 2.5H$ with χ and Am being around 1, and the range of influence by AD extends higher from the midplane than the Hall effect. The Hall effect is less important relative to AD with stronger net flux $\beta_0 = 10^4$ because the resulting total field is stronger. Beyond $z \sim 2.5H$, the FUV ionization catches up and all non-ideal MHD effects are greatly reduced. Beyond $z = \pm 3H$, the gas essentially behaves in the ideal MHD regime with $Am > 100$.

Vigorous MRI turbulence takes place beyond about $z \sim \pm 2.5H$ thanks to FUV ionization. As a result, the profile of the Maxwell stress $T_{R\phi}^{\text{Max}} = -B_x B_y$ peaks at around $z = \pm 3H$, as shown in the top right panel of Figure 6 and middle panel of Figure 7. Beyond $z \sim \pm 3H$, the Maxwell stress drops because disk density drops and it enters the magnetically dominated corona (plasma $\beta < 1$). All three runs at a given β_0 show very similar properties in this region, since the gas behaves in

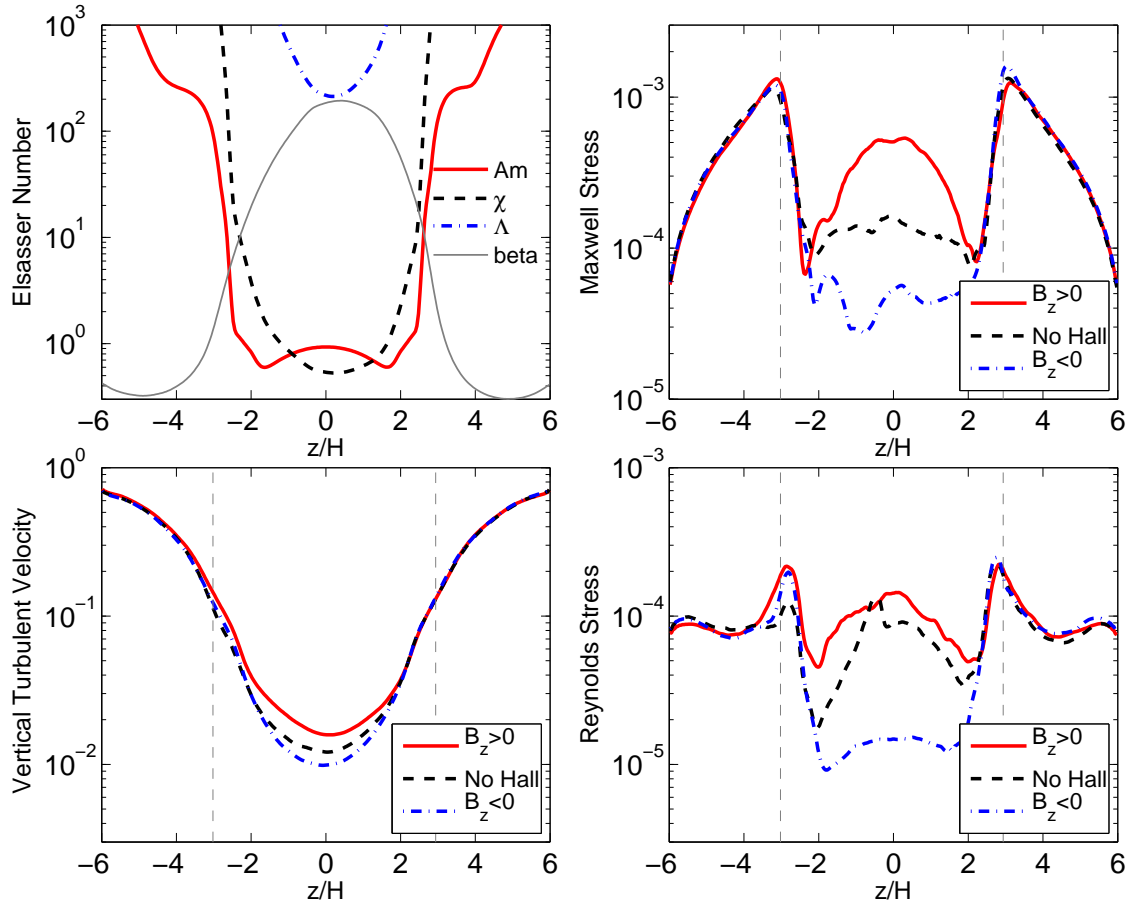


FIG. 6.— The vertical profiles of various horizontally averaged diagnostic quantities from our runs at 30 AU with $\beta_0 = 10^5$. Top left: the Ohmic (Λ), Hall (χ) and ambipolar (Am) Elsasser numbers in blue dash-dotted, black dashed and red solid lines, together with plasma β in thin gray line. The profile is extracted from the Hall-free run R30b5H0 (almost identical to the other two runs). Bottom left: vertical turbulent velocity. The rest three panels show various profiles for all three runs of R30b5H+ (red solid), R30b5H0 (black dashed) and R30b5H- (blue dash-dotted). Top right: Maxwell stress $-B_x B_y$. Bottom right: Reynolds stress $\rho v_x v_y$. The gray vertical dashed lines mark the location where $Am = 100$ in run R30b5H0.

the ideal MHD regime. Runs with $\beta_0 = 10^4$ have systematically higher Maxwell stress than the corresponding $\beta_0 = 10^5$ runs by a factor of 3-4 as a result of stronger background field.

The midplane region is where three simulations at fixed β_0 are expected differ due to the Hall effect. The most prominent difference lies in the Maxwell stress. The runs with $B_{z0} > 0$ give the highest stress that peaks at the midplane. This is related to the Hall-shear instability (Kunz 2008), which operates only when $B_{z0} > 0$, and is responsible for generating stronger horizontal magnetic fields hence Maxwell stress in the inner disk (Lesur et al. 2014, paper I). Here, the effect is much less prominent than in the inner disk studied in paper I and Lesur et al. (2014) since the Hall effect is only modestly significant ($\chi \sim 1$). The runs with $B_{z0} < 0$ give the lowest midplane Maxwell stress, while the Maxwell stress from R30b5H0 (without the Hall term) lies in between. This is again consistent with the expectation from paper I that horizontal magnetic field tends to be reduced for negative B_{z0} .

As discussed in Section 2, for $B_{z0} > 0$, the midplane region is unstable to the MRI, and the level of the MRI turbulence is expected to be stronger than the Hall-free case. For $B_{z0} < 0$, self-sustained MRI turbulence is not

expected due to the Hall effect. To characterize the level of turbulence, we consider the vertical component of the rms velocity, which are shown in the bottom left panel of Figure 6 and the right panel of Figure 7 for the two sets of runs. They are computed based on the turbulent kinetic energy at each height. In the same way, we define δv_z to be the rms vertical velocity fluctuation within $z = \pm 2H$ for all our runs, and have included it in Table 2.

We see that the turbulent rms vertical velocity reaches $\sim 0.3 - 0.8c_s$ at disk surface ($z \sim \pm 4H$) for all these runs, while is reduced by more than one order of magnitude to $\sim 0.01 - 0.03c_s$ around disk midplane. For $\beta_0 = 10^5$, the run with $B_{z0} > 0$ gives higher midplane turbulent velocity while the run with $B_{z0} < 0$ gives the lowest, and the Hall-free run lies in between, which is consistent with our expectation. Nevertheless, the difference is within a factor of 2, hence the role of the Hall effect in the midplane turbulent activities is only modest. While we caution that the level of turbulence in the $B_{z0} > 0$ case may be underestimated due to the lack of numerical resolution, the overall scenario is similar to the Hall-free case, and consistent with earlier stratified AD simulations of (Simon et al. 2013a), where the midplane region was termed as ‘‘ambipolar-damping’’ zone (the region MRI active but with low turbulence level due

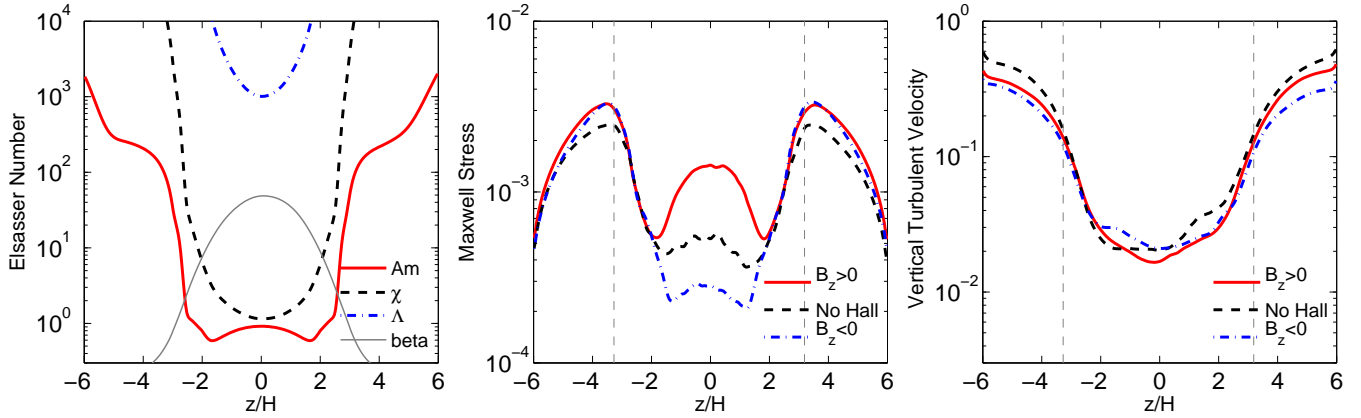


FIG. 7.— Same as the Figure 6 without the bottom right panel, but for runs at 30 AU with $\beta_0 = 10^4$. The vertical dashed line labels the location where $Am = 100$ in run R30b4H0.

to AD). In the case of $B_{z0} < 0$ where MRI can not be self-sustained at disk midplane, the midplane turbulent motion is most likely induced by the strong MRI turbulence in the disk surface layer, which is a direct analog of the *conventional* “Ohmic dead zone” the inner disk (e.g., Fleming & Stone 2003; Oishi & Mac Low 2009).

For $\beta_0 = 10^4$, we find that the level of midplane turbulence in all three runs are very similar (modulo some secular variations not reflected in the time-averaged plots), despite the marked difference in Maxwell stress. We have checked that for $B_{z0} > 0$, the midplane Maxwell stress is dominated by contributions from large-scale field ($-\overline{B_x B_y}$), while for $B_{z0} < 0$, the midplane Maxwell stress is almost entirely due to turbulent field. Turbulent contributions of the midplane Maxwell stress from the two runs R30b4H+ and R30b4H- are in fact similar. We have also checked that for $\beta_0 = 10^5$, midplane Maxwell stress is always dominated by turbulent stress. The low level of turbulence in run R30b4H+ may be considered as a consequence of the strong mean toroidal field ($\overline{B_y}$), which dominates the magnetic field strength and tends to suppress turbulent motions (but see also Section 4.4).

Overall, based on the six simulations with different strengths and polarities of the net vertical field, it is clear that the Maxwell stress profile (hence radial transport of angular momentum) is layered. Moreover, it appears that $\delta v_z \approx 0.01 - 0.02 c_s$ is a good proxy for the level of turbulence in the midplane region of the outer disks, with much stronger turbulence in the FUV ionization layer at disk surface.

4.3. Angular Momentum Transport and Disk Outflow

Outflow is always launched in shearing-box simulations in the presence of net vertical magnetic flux (e.g., Suzuki & Inutsuka 2009). While this outflow may serve as a wind launching mechanism, the kinematics of the outflow is not well characterized in shearing-box simulations because the rate of the mass outflow does not converge with simulation box height (Fromang et al. 2013) and there are also symmetry issues (Bai & Stone 2013a). Therefore, we do not aim at fully characterizing the outflow properties, but simply provide some basic diagnostics for reference. We calculate the rate of mass outflow leaving the simulation box \dot{M}_{out} . It is computed by time

averaging the sum of vertical mass flux at the two vertical boundaries. We also calculate the $z\phi$ component of the Maxwell stress tensor $T_{z\phi}^{\text{Max}} = -B_z B_\phi$, which determines the rate of wind-driven angular momentum transport (if the outflow is eventually incorporated into a global magnetocentrifugal wind). In the laminar case, $T_{z\phi}$ can be conveniently evaluated at the base of the wind where the toroidal velocity transitions from sub-Keplerian to super-Keplerian (Bai & Stone 2013b; Bai 2013). Since most of our simulations runs are highly turbulent at the disk surface, there are ambiguities in defining the base of the wind (and whether the outflow can become a global wind at all, Bai & Stone 2013a), we simply provide a reference value of time-averaged $|T_{z\phi}^{\text{Max}}|$ evaluated at $z = \pm 4.5H$ in Table 2.

The value of Shakura-Sunyaev α for stratified disk can be written as

$$\alpha = \frac{\int T_{R\phi} dz}{c_s^2 \int \rho dz}, \quad (12)$$

where $T_{R\phi}$ has contributions from both the Maxwell stress ($-B_x B_y$) and Reynolds stress ($\rho v_x v_y$), leading to α^{Max} and α^{Rey} in Table 2. From the lower right panel of Figure 4, we see that the vertical profile of the Reynolds stress is generally a factor of several smaller than the Maxwell stress. Due to uncertainties in characterizing the outflow from shearing-box simulations, we truncate the vertical integral at $z = \pm 4.5H$. For the six runs, the values of α are found to be around $1.5 - 2 \times 10^{-3}$ for $\beta_0 = 10^5$ and $5 - 6 \times 10^{-3}$ for $\beta_0 = 10^4$.

In steady state, the total accretion rate driven from radial transport of angular momentum (given by α) and the putative wind-driven accretion (given by $T_{z\phi}$) can be approximately written as (e.g., Bai 2013)

$$\begin{aligned} \dot{M} &\approx \frac{2\pi}{\Omega} \alpha c_s^2 \Sigma + \frac{8\pi}{\Omega} R |T_{z\phi}|, \\ \dot{M}_{-8} &\approx 0.82 \left(\frac{\alpha}{10^{-3}} \right) R_{\text{AU}}^{-1/2} + 4.1 \left(\frac{|T_{z\phi}|}{10^{-4} \rho c_s^2} \right) R_{\text{AU}}^{-3/4}, \end{aligned} \quad (13)$$

where R_{AU} is the radius measure in AU, and we have assumed MMSN disk model in the second equation, with \dot{M}_{-8} being accretion rate measured in $10^{-8} M_\odot \text{ yr}^{-1}$.

Using the values from Table 2 with $R = 30 \text{ AU}$, we find

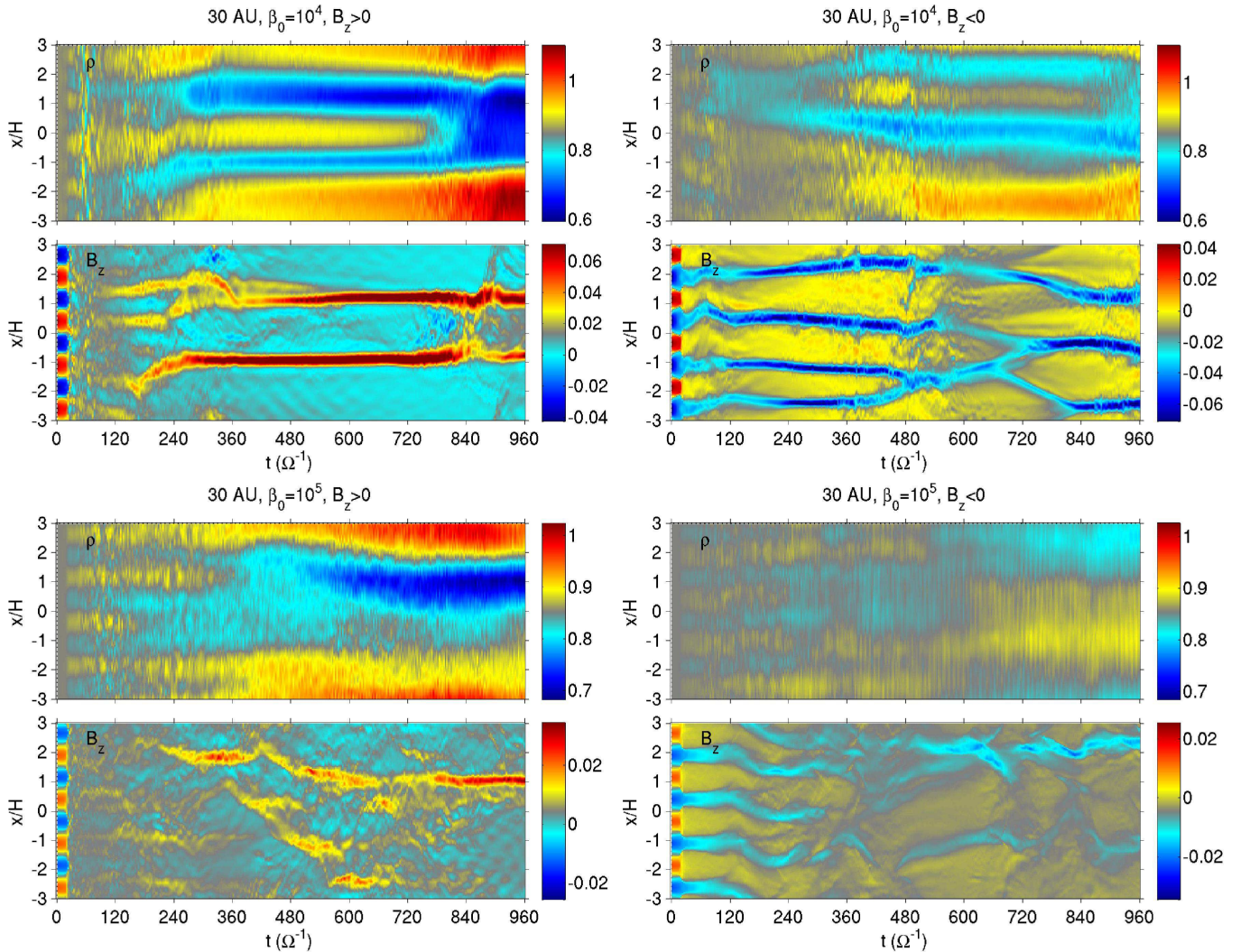


FIG. 8.— Time evolution of the radial profiles of mean gas density ρ (upper panels) and mean vertical magnetic field B_z (lower panels) averaged over the $y-z$ plane within $z = \pm 2H$ in our runs R30b4H+ (upper left), R30b4H- (upper right), R30b5H+ (lower left) and R30b5H- (lower right). The color scales are centered in their mean values (in code units).

that based on radial transport alone, the resulting accretion rate is about $0.24 - 0.33 \times 10^{-8} M_{\odot} \text{ yr}^{-1}$ for the three runs with $\beta_0 = 10^5$ studied here, which is somewhat smaller than desired. If there were contributions from disk wind, the estimated wind-driven accretion rate is about $0.7 \times 10^{-8} M_{\odot} \text{ yr}^{-1}$. The sum of the two contributions just matches the desired rate of $10^{-8} M_{\odot} \text{ yr}^{-1}$. For $\beta_0 = 10^4$, accretion rate resulting from radial angular momentum transport gives $\sim 0.72 - 0.91 \times 10^{-8} M_{\odot} \text{ yr}^{-1}$, with potential contribution from the wind to give $\sim 5 \times 10^{-8} M_{\odot} \text{ yr}^{-1}$.

4.4. Zonal Field and Zonal Flow

For our 30 AU simulations, we find using Equation (8) and from the Elsasser number plots in Figures 6 and 7 that $l_H \approx 0.2H$ around disk midplane, which is about the threshold value to trigger the zonal field configuration in the unstratified case as discussed in Kunz & Lesur (2013). In Section 2 we showed in Figure 3 that strong zonal field and zonal flow is observed in unstratified simulations when $\beta_0 = 10^4$ and $B_{z0} > 0$. To check whether

our stratified simulations reveal similar behaviors, we show in Figure 8 the time evolution of mean gas density ρ and B_z for runs 30Aub4H \pm and 30Aub5H \pm , averaged in the y and z dimensions, within the disk region $-2H \leq z \leq 2H$.

We find that strikingly, for all runs, vertical magnetic flux is concentrated into thin (azimuthally extended) shells, while in regions outside these shells, the net vertical flux is close to zero. In the mean time, there are very prominent radial density variations characteristic of strong zonal flow. There are clearly secular evolution of the vertical magnetic flux distribution and zonal flows, which is also related to the secular behaviors discussed in Section 4.1. At first glance, these features appear to be consistent with those shown in Figure 3 from our unstratified simulations. However, there are distinct differences. In particular, both $B_{z0} > 0$ and $B_{z0} < 0$ cases show such zonal fields, while from unstratified simulations zonal field is expected only from the $B_{z0} > 0$ case. Also, the width of the zonal field is very small ($< 0.5H$), while from unstratified simulations the width is generally wider than H .

In fact, we find that concentration of magnetic flux appears to be a generic behavior in shearing-box simulations with net vertical magnetic flux. Not only in simulations with the Hall effect, but our Hall-free simulations at 30 AU, together with many simulations at other disk radii, all show this behavior to some level. We also find that the concentration is less prominent when the net vertical field is weaker, as one compares the top and bottom panels in Figure 8. Accompanied with magnetic flux concentration is the strong zonal flow, which density variation across the domain up to $\sim 30\%$. Enhanced zonal flow in the presence of net vertical magnetic flux was reported in Simon & Armitage (2014) based on stratified shearing-box simulations in the AD dominated outer disk. Such zonal flows also exist in our earlier simulations including both Ohmic resistivity and AD further closer in (at 10-20 AU, Bai 2013), and we have verified that in general, there is only one single “wavelength” of the density/pressure variation across the radial domain, regardless of the radial domain size (Bai, 2013, unpublished). From Figure 8, we see that the location where magnetic flux concentrates significantly correlates with the density minimum. While less evident in run R30b4H– (the trend weakens in the $B_{z0} < 0$ case due to the Hall effect), in general, the enhanced zonal flow is directly associated with the magnetic flux concentration.

In sum, the zonal field and zonal flow observed in our stratified simulations are not due to the Hall effect as reported in unstratified simulations, but are correlated phenomenon generically present in shearing-box simulations with net vertical magnetic flux. While the saturation of the zonal flow is artificially affected by the shearing-box since its radial scale is set by the simulation box size, its association with magnetic flux concentration may make it very likely a physical phenomenon. Our local simulations here serve as a first study of the PPD gas dynamics including all non-ideal MHD effects, and it remains to understand their underlying physics and verify their existence in global simulations.

5. SIMULATIONS AT 5 AU

Our second focused location is at relatively small radius of $R = 5$ AU, which compliments our studies in paper I⁴. Using quasi-1D simulations, we have found in paper I that for $B_{z0} > 0$, the inner disk launches a laminar magnetocentrifugal wind which very efficiently drives disk accretion. In constructing the wind solutions, we enforced reflection symmetry about disk midplane so that the wind solution has the desired symmetry properties to match to a physical magnetocentrifugal wind (i.e., horizontal component of the magnetic field must flip across the disk). It remains to demonstrate that this wind configuration is stable in 3D without enforcing the symmetry. Another important result from paper I is that for $B_{z0} < 0$, we did not find any stable wind configuration for typically expected level of vertically magnetic field strength at this location ($\beta_0 = 10^{5-6}$) since MRI sets in in a very narrow range of disk height. It remains to demonstrate how the disk behaves under this situation.

⁴ To better compare with the results in paper I, we runs the simulations at 5 AU with the same vertical outflow boundary condition as paper I instead of the modified version in the rest of the simulations.

We have performed three runs. For $B_{z0} > 0$ we consider $\beta_0 = 10^5$ (run R5b5H+), while for $B_{z0} < 0$ we consider $\beta_0 = 10^5$ and 10^4 (runs R5b5H– and R5b4H–). From paper I, we expect largely laminar configurations to be developed for runs R5b5H+ and R5b4H–, launching magnetocentrifugal wind; while the MRI should set in for run R5b5H–. In Figure 9, we again show the time evolution of the horizontally averaged B_y in the three runs. Given the highly regular patterns seen in this Figure, it suffices to run these simulations just to $t = 360\Omega^{-1}$ and perform time average from $t = 180\Omega^{-1}$ onward.

5.1. Simulation with $B_{z0} > 0$

For run R5b5H+, we see from the top panel of Figure 9 that the system is able to achieve a largely laminar state as desired. More interestingly, the toroidal field changes sign almost exactly at the disk midplane, automatically maintaining the reflection symmetry (more specifically, even- z symmetry, see Figure 9 of Bai & Stone 2013b). Achieving this field geometry is essential for physically launching a magnetocentrifugal wind, and supports the procedure adopted in paper I where the reflection symmetry across midplane was enforced. Checking the time-averaged vertical profiles of various quantities, we find that the result is almost identical with Figure 9 of paper I (with slight difference since our box extends to $z = 6H$ rather than $8H$). For this solution, the horizontal magnetic field near the midplane is strongly amplified by the Hall shear instability, and the flip of this horizontal field creates strong current density at the midplane. This contrasts with the study by Bai (2013), where without the Hall term, the strong current layer was found to be located offset from the midplane at $z_{SC} \approx 1.3H$ in this particular case (see his Table 2 for run S-R5-b5). It appears that with the inclusion of the Hall term, horizontal magnetic field tends to flip right across the midplane, rather than from upper layers.

In Figure 10 we further show the vertical profiles of time-averaged Maxwell stress and vertical turbulent velocities. For our run R5b5H+, we see that the Maxwell stress profiles peaks close to disk midplane at rather high level close to $10^{-2}\rho_0 c_s^2$. The dip at midplane is due to the flip of horizontal field, all in agreement with the results in paper I. For the profile on turbulent velocity, however, we find that appreciable level of turbulence is present in this run. The turbulent velocity is again on the order of $0.01c_s$ around the midplane, and increases toward surface layer at a level very similar to that in the outer disk studied in the previous section. Since we expect the system to be stable to the MRI, the turbulence mainly originates from elsewhere: at the midplane, we find that the strong current layer tends to exhibit small amplitude corrugation from time to time resembling the tearing modes in reconnection current sheet. Such corrugating motion is likely the source of most random velocities which propagates toward disk surface layers and becomes amplified due to rapid density drop.

In sum, for $B_{z0} > 0$, our 3D simulation with full box well reproduces the quasi-1D simulations with enforced reflection symmetry in paper I, and we expect accretion is mainly driven by magnetocentrifugal wind, together with significant contribution from radial transport of angular momentum via the large-scale Maxwell stress/magnetic

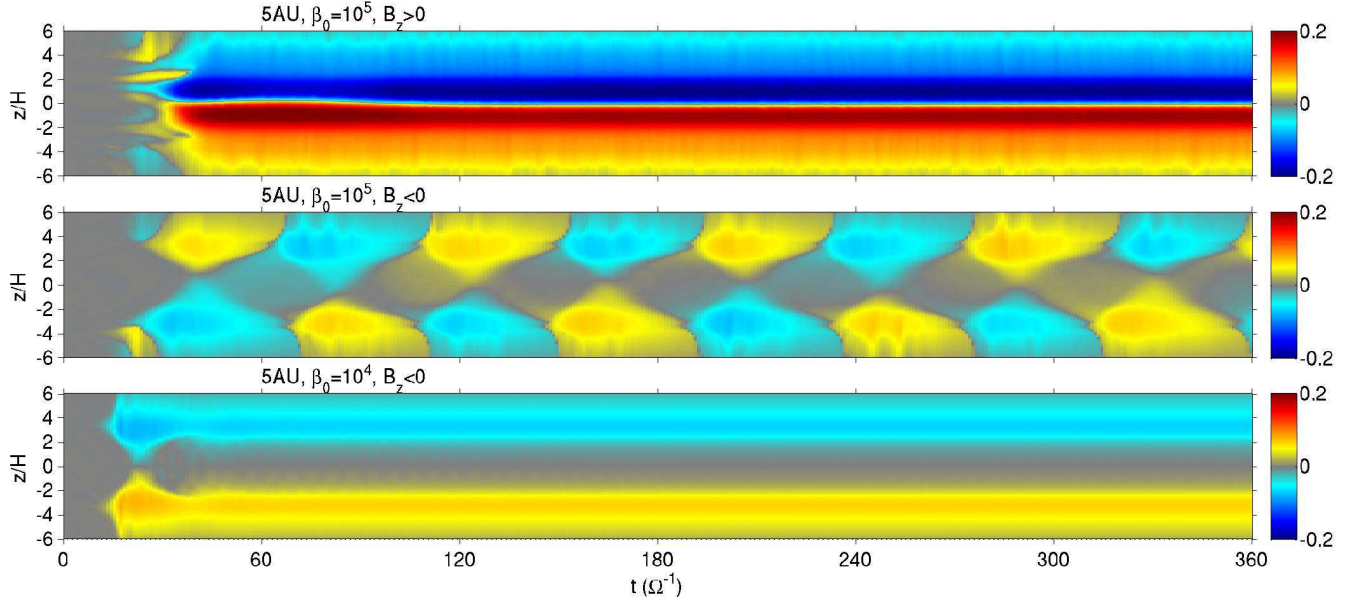


FIG. 9.— The time evolution for the vertical profile of horizontally averaged B_y in our runs at 5 AU. The top, middle and bottom panels correspond to runs R5b5H+, R5b5H– and R5b4H–.

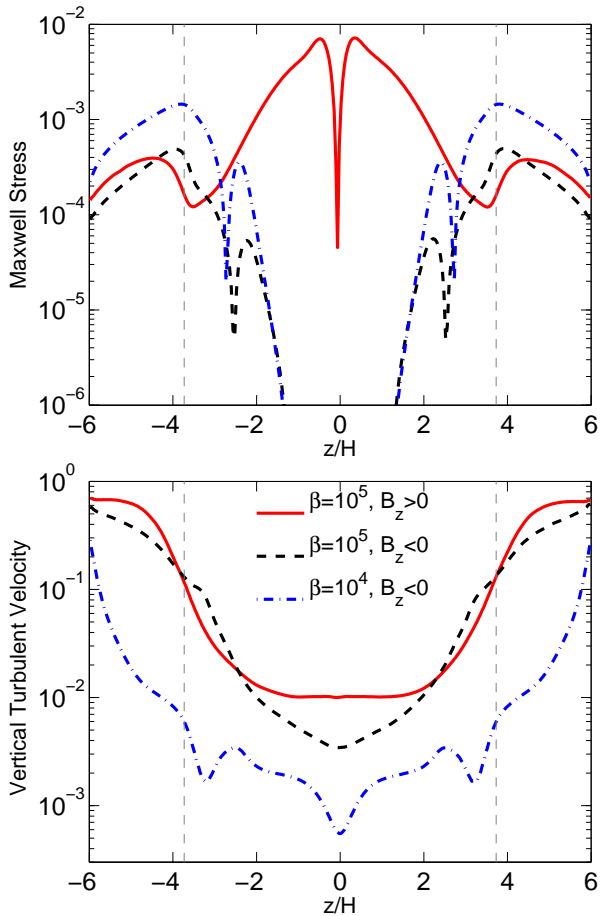


FIG. 10.— Vertical profiles of Maxwell stress (top) and vertical turbulent velocity (bottom) for all three runs at 5 AU, as marked in the legend. The vertical dashed line labels the location where $Am = 100$ in run R5b5H–.

braking (see Table 2 of paper I). The wind-driven accretion flow mostly proceeds in the strong current layer where toroidal magnetic field flips (Bai & Stone 2013b), and here it takes place exactly at disk midplane. Our 3D simulation further reveals the presence of turbulence, which largely originates from the midplane region where relatively strong large-scale horizontal magnetic fields flip. The level of turbulence is similar to that in the outer disk. We also comment that since the system is stable to the MRI, magnetic flux concentration into thin shells is not observed in this simulation.

5.2. Simulations with $B_{z0} < 0$

For run R5b5H–, the system is expected to be unstable to the MRI in a narrow range of disk height at about $|z| \sim 2 - 3H$. This can roughly be identified from the left panel of Figure 9 in paper I, where the Hall Elsasser number passes 1 at around $z = 2.5H$ and plasma β is still not too small (based on the Hall-free run in dashed lines). Detailed explanation on the onset of the instability is given in Section 5.2 of paper I, but in brief, it is related to the fact that for $B_{z0} < 0$, the Hall term makes the most unstable MRI wavelength shifts to shorter wavelength when Elsasser number χ_0 is of order unity, allowing the unstable modes to fit into the disk. Using full 3D simulations, we see from the middle panel of Figure 9 that the large-scale toroidal magnetic field flips in highly periodic manner, and the origin of the periodic flips directly connects to the unstable region. Interestingly, the toroidal field in the upper and lower halves always have opposite signs, and the midplane horizontal field is very weak (and goes through zero). We have also found that the overall mean field evolution can be almost exactly reproduced from our quasi-1D simulation of paper I. An outflow is launched, whose mass outflow rate is smaller than but the same order of magnitude to the rate from our run R5b5H+ (see Table 2). Therefore, at a given time, the magnetic field configuration can be considered physical for a magnetocentrifugal wind. However, since

the toroidal (hence radial) field constantly changes sign, the wind keeps oscillating between radially inward and outward directions, a fact that is inconsistent with global wind geometry, and reflects the limitation of the local shearing-box framework (Bai & Stone 2013a). While the periodic field flips are likely physical phenomenon inherent with the onset of the MRI, global simulations are necessary to determine the fate of the outflow.

The onset of the MRI also leads to some level of turbulence, as seen from the bottom panel of Figure 10. Beyond the region where MRI operates, turbulent motion largely results from passive response to the MRI activities, and the midplane has the weakest level of turbulent motion. Despite different origins, the level of turbulence is comparable to run R5b5H+, especially at the surface.

The fact that mean toroidal field periodically changes sign makes it ambiguous to estimate the role of disk wind in transporting angular momentum (net wind-driven accretion rate would be zero considering the periodic flips). Here we set it aside and look at the radial transport of angular momentum from the Maxwell stress, as shown in the top panel of Figure 10. We see that Maxwell stress peaks at about $|z| \sim 4H$, but at a relatively low level. We estimate the total α to be only about 4.5×10^{-4} , corresponding to accretion rate of $\sim 1.6 \times 10^9 M_\odot \text{ yr}^{-1}$ using Equation (13). This is about an order of magnitude smaller than the expected level of $10^{-8} M_\odot \text{ yr}^{-1}$.

We further performed run R5b4H- with stronger net vertical field $\beta_0 = 10^4$. Based on paper I, we expect the system to be stable to the MRI and develop a laminar magnetocentrifugal wind. This is again confirmed using full 3D simulations, with the general wind properties almost identical to the one obtained in paper I. In particular, our full 3D run automatically obeys the reflection symmetry across the midplane, confirming that solutions with enforced symmetry in paper I are generally physical. Note that toroidal field is close to zero near the midplane as a result of the Hall term. The level of random motion in our run R5b4H- is systematically weaker than all other runs, confirming its intrinsically laminar nature. One can read from Table 2 to obtain the Maxwell stress as well as the wind stress to derive the accretion rate resulting from radial transport and wind, or directly look from Table 2 of paper I for more accurate estimates. We see that radial transport is completely negligible compared with wind-driven accretion rate, which gives the value of $\sim 10^{-7} M_\odot \text{ yr}^{-1}$, and is an order of magnitude more than sufficient.

In sum, it appears that for $B_{z0} < 0$, while results from our shearing-box simulations are likely robust, they also raise puzzling issues regarding the mechanism to transport angular momentum. For relatively weak net vertical field ($\beta_0 \sim 10^5$), MRI sets in, leading to a periodically oscillating outflow where based on shearing-box simulations we are unable to tell if it drives angular momentum transport; but radial transport of angular momentum by Maxwell stress appears too inefficient. For relatively strong net vertical field ($\beta_0 \sim 10^4$), the system unambiguously launches the magnetocentrifugal wind which drives very rapid accretion with higher accretion rate than typically observed. At this point it is unclear how the system can achieve accretion rate at the desired rate

of $\sim 10^{-8} M_\odot \text{ yr}^{-1}$, an issue that can only be clarified from global simulations.

6. SIMULATIONS AT OTHER DISK RADII

In this section, we further perform simulations at two other locations, 15 AU and 60 AU, from which we study the radial dependence of PPD gas dynamics and the role played by the Hall effect. At each location, we perform four simulations with $\beta_0 = 10^4$ and 10^5 and different magnetic polarities, where all non-ideal MHD terms are turned on.

6.1. Results from 15 AU

At 15 AU, our quasi-1D simulations suggest laminar configuration for $B_{z0} > 0$ with $\beta_0 = 10^4$, but more turbulent situation is expected otherwise. In Figure 11 we show the overall time evolution of the horizontally averaged toroidal field. In Figure 12 we further show the time averaged profiles of Maxwell stress and vertical turbulent velocity for all four runs, where the time averages are taken from time $t = 420\Omega^{-1}$ onward. We see that for all four runs, the system eventually settle into a state where the large-scale toroidal field remains one sign across the entire disk, hence the symmetry of the outflow would be undesirable for a global wind. Nevertheless, we again set aside on the issue with symmetry and focus on other properties.

For $B_{z0} > 0$ and comparing runs R15b5H+ with R15b4H+, it is counterintuitive to notice from both Figures that stronger mean toroidal magnetic field is generated when the net vertical field is weaker (R15b5H+), leading to stronger Maxwell stress around disk midplane. Looking into the entire simulation data reveal that for run R15b4H+, essential all the vertical magnetic flux is concentrated into a single thin shell, while the rest of the radial zones have effective zero net vertical flux. As a result, magnetic field amplification by the Hall shear instability is suppressed for the bulk of the disk. A strong zonal flow is also formed with high density contrast of 30% where shell of magnetic flux locates at the density minimum. The highly non-uniform distribution of magnetic flux also makes the gas dynamics in this run deviate from the wind solution in paper I (see his Table 2). On the other hand, for run R15b5H+, magnetic flux distribution is much more uniform, leading to effective growth of horizontal magnetic field due to the Hall shear instability, producing stronger Maxwell stress at disk midplane. Again, it is unclear at this point how realistic the level of magnetic flux concentration is, hence the results shown here should be treated with caution.

For $B_{z0} < 0$, we see that the initial evolution of the mean toroidal field closely resembles our run R5b5H-, with quasi-periodic flips and the top and bottom sides possesses opposite sign of mean B_y . This is again because the MRI sets in in the layer where the Hall Elsasser number transitions through order unity. Later on, field of one sign takes over and dominates the entire disk. There are also MRI activities in the FUV layer, though the level is weaker than their 30 AU counterpart (e.g., seen from the peak Maxwell stress). To some extent, this location represents a transition between the 5AU and 30 AU cases, where in the former MRI is triggered mainly in the Hall dominated layer while in the latter MRI is

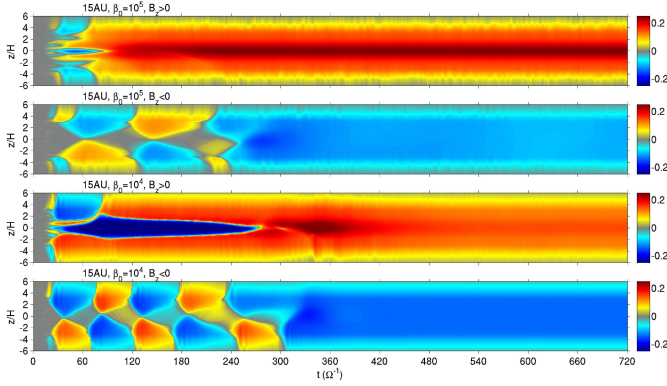


FIG. 11.— The time evolution for the vertical profile of horizontally averaged B_y in our runs at 15 AU. Shown from top to bottom are runs R15b5H+, R15b5H-, R15b4+ and R15b4H-.

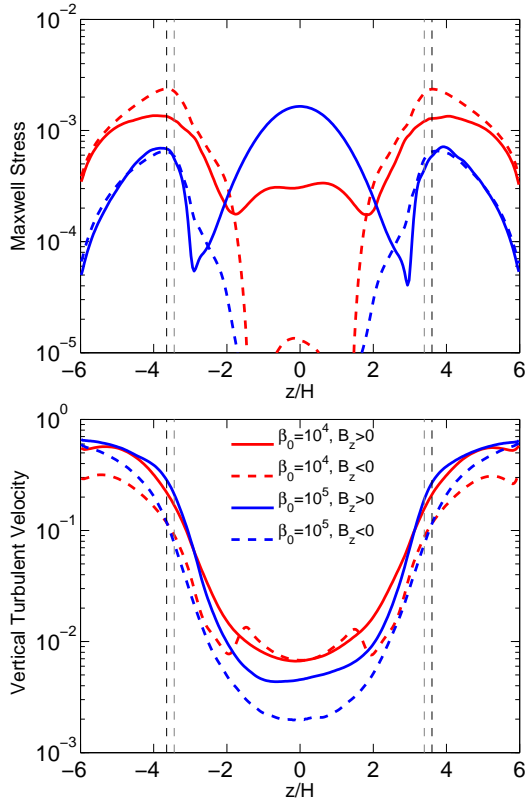


FIG. 12.— Vertical profiles of Maxwell stress (top) and vertical turbulent velocity (bottom) for all four runs at 15 AU, as marked in the legend. The vertical dashed lines mark the location where $Am = 100$ in run R15b4H- (dark) and R15b5H- (light).

active mainly in the FUV layer. As usual, the horizontal magnetic field is suppressed due to the Hall effect, and most of the Maxwell stress originates from the FUV layer.

From the value of α^{Max} and $T_{z\phi}^{\text{Max}}$ listed in Table 2 and using Equation (13), we see that the net vertical magnetic flux has to be at least $\beta_0 = 10^4$ in order for the accretion rate to reach levels comparable to $10^{-8}M_{\odot} \text{ yr}^{-1}$. On the other hand, if magnetocentrifugal wind is operating, the level of $T_{z\phi}^{\text{Max}}$ from weak net vertical field with $\beta_0 = 10^5$ is sufficient drive accretion rate above the

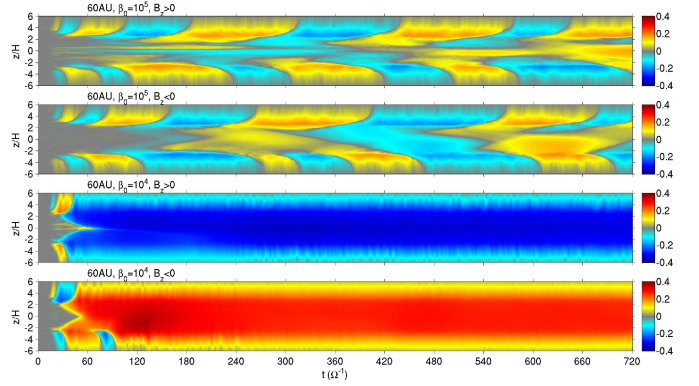


FIG. 13.— The time evolution for the vertical profile of horizontally averaged B_y in our runs at 60 AU. Shown from top to bottom are runs R60b5H+, R60b5H-, R60b4+ and R60b4H-.

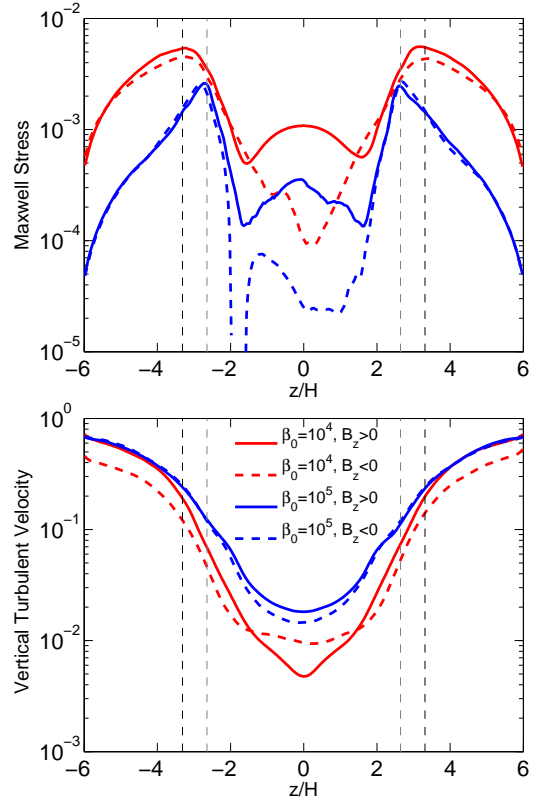


FIG. 14.— Vertical profiles of Maxwell stress (top) and vertical turbulent velocity (bottom) for all four runs at 60 AU, as marked in the legend. The vertical dashed lines mark the location where $Am = 100$ in run R60b4H- (dark) and R60b5H- (light).

desired level. Overall, turbulent velocity is smallest at midplane either due to weak MRI turbulence ($B_{z0} > 0$ with weak field) or induced random motion from MRI activities in the disk surface ($B_{z0} < 0$), similar to the 30 AU case.

6.2. Results at 60 AU

At 60 AU, the relative importance of the Hall effect is reduced by a factor of ~ 2 compared with the 30 AU case (see Equation 9), and is only marginally important at disk midplane. AD is the dominant effect in most regions of the disk. Also, given the approximately con-

stant penetration column density of the FUV ionization, it effectively penetrates deeper at the more tenuous outer disk in terms of disk scale height. In Figure 13 we show the overall time evolution of the horizontally averaged toroidal field. In Figure 14 we further show the time averaged profiles of Maxwell stress and vertical turbulent velocity for all four runs, where the time averages are taken from time $t = 300\Omega^{-1}$ onward. The general evolution of the system is in many ways similar to our focused study at 30 AU, where MRI drives vigorous turbulence in the surface FUV layer, with the midplane region only weakly turbulent. Here we mainly focus on the differences and the overall trend toward larger disk radii.

At $\beta_0 = 10^5$, dynamo activities constantly flip the mean toroidal field similar to but appears more regular than the 30 AU case for both magnetic polarities. For $\beta_0 = 10^4$, the dynamo is suppressed and the entire disk is dominated by a mean toroidal field with a single sign. When $B_{z0} < 0$, we do not observe the mean field changing sign as the 30 AU counterpart shown in Figure 5. In fact the toroidal field in the entire disk has the same sign throughout the saturated state of the simulation hence we do not expect this sign flip to occur. We speculate that the flip we observed at 30 AU is associated with the relatively strong Hall effect at the disk midplane, but it is unlikely to occur toward the outer disk as the Hall effect becomes less dominant.

At 60 AU, the contrast in Maxwell stress between the $B_{z0} > 0$ and $B_{z0} < 0$ cases at disk midplane is still very evident. Level of turbulence is found to be higher for runs with weaker net vertical field $\beta_0 = 10^5$, which may be due to the fact that in runs with $\beta_0 = 10^4$, turbulent motion is limited by the relatively strong large-scale toroidal field, but it may also be due to strong concentration of magnetic flux into thin shells where a large fraction of the simulation domain has effectively zero net vertical flux.

Deeper penetration of FUV ionization allows the MRI to be fully active over thicker surface layers, hence the Maxwell stress profiles at disk surface at fixed β_0 is higher than their 30AU counterparts, giving larger values of α^{Max} . Again, we find that for the Maxwell stress alone to drive accretion rate of $\sim 10^{-8}M_{\odot} \text{ yr}^{-1}$, the net vertical flux needs to be $\beta_0 \sim 10^4$ or stronger. The magnetocentrifugal wind, if operating in the outer disk, would drive accretion with rate $\sim 0.4 - 4 \times 10^{-8}M_{\odot} \text{ yr}^{-1}$ for $\beta_0 = 10^5$ to 10^4 .

7. SUMMARY AND DISCUSSIONS

7.1. Summary

In this work, we have studied the gas dynamics of PPDs focusing on regions toward the outer disk (from 5-60 AU), taking into account all non-ideal MHD effects in a self-consistent manner. In these regions, the Hall effect generally dominates near the disk midplane, and ambipolar diffusion (AD) plays an important role over a more extended region across disk height, and the very surface layer behaves in the ideal MHD regime due to FUV ionization. In the presence of the Hall effect, the gas dynamics depends on the polarity of the large-scale vertical/poloidal magnetic field (B_{z0}) threading the disk relative to the rotation axis (along \hat{z}). Since the relative

importance of the Hall effect to AD gets progressively weaker with increasing disk radius, we estimate based on the MMSN disk model that the Hall-effect controlled polarity dependence extends to about 60 AU.

We first conducted unstratified MRI simulations including both the Hall effect and AD. We find that at conditions expected in the outer region of PPDs (midplane plasma β_0 for the net vertical field being 10^{4-5}), MRI leads to turbulence when $B_{z0} > 0$ but can not be self-sustained for $B_{z0} < 0$. For $B_{z0} > 0$, the level of MRI turbulence is of the order $\alpha \sim 10^{-3}$ (with AD Elsasser number $Am = 1$). We confirm that strong zonal field configuration of Kunz & Lesur (2013) can be achieved with sufficiently strong Hall effect, and find that in the mean time it leads to strong zonal flows. In addition, numerical resolution of 24 cells per $H = c_s/\Omega$ is in general sufficient to resolve the bulk properties of the MRI turbulence.

We then focused on self-consistent stratified MRI simulations at fixed disk radius, with main results summarized as follows.

At relatively small disk radius (~ 5 AU), and for $B_{z0} > 0$, we confirm and justify the results from paper I that the system launches a strong magnetocentrifugal wind, and is able to achieve a physical wind geometry, with the horizontal magnetic field flips exactly at disk midplane. While Maxwell stress is enhanced due to the Hall shear instability, accretion is largely driven by the wind and proceeds primarily through the midplane. In addition, the midplane region is weakly turbulent which is likely resulting from the flip of relatively strong horizontal magnetic field. The turbulent motion gets amplified toward disk surface as gas density drops.

For $B_{z0} < 0$, our full 3D simulations confirm results from paper I that the system is unstable to the MRI in thin Hall-dominated layers when net vertical field is relatively weak ($\beta_0 = 10^5$). This results in periodic flips of large-scale horizontal magnetic field over time with a radially oscillating disk outflow/wind whose fate and whether it drives accretion are uncertain based on shearing-box simulations. Radial transport of angular momentum by Maxwell stress is found to be too inefficient by an order of magnitude. A stable magnetocentrifugal wind with physical wind geometry can be achieved with stronger net vertical field ($\beta_0 = 10^4$), which very efficiently drives accretion with $\dot{M} \gtrsim 10^{-7}M_{\odot} \text{ yr}^{-1}$. It is uncertain whether and how the system can achieve the typically observed rate of $10^{-8}M_{\odot} \text{ yr}^{-1}$.

At relatively large disk radius (~ 30 AU), we find that the Hall effect mainly affects the Maxwell stress at disk midplane, with $B_{z0} > 0$ ($B_{z0} < 0$) giving enhanced (reduced) stress similar to those found at the inner disk (paper I, Lesur et al. 2014). Nevertheless, strongest Maxwell stress results from vigorous MRI turbulence in the surface layer due to FUV ionization (Perez-Becker & Chiang 2011; Simon et al. 2013a). While self-sustained MRI is expected at disk midplane when $B_{z0} > 0$ but not when $B_{z0} < 0$, the level of turbulence in these cases appears very similar, with vertical turbulent velocity of the order $\delta v_z \sim 0.01 - 0.03c_s$. The turbulent motion in the latter case is largely induced

from stronger turbulence in the surface layer analogous to the conventional “Ohmic dead zone” picture (e.g., Fleming & Stone 2003). Overall, the gas dynamics in the outer regions of PPDs show clear layered structure consisting of highly turbulent surface FUV ionization layer with strong Maxwell stress and weakly turbulent mid-plane region due to a combination of AD, the Hall effect and large-scale magnetic field structure.

We find that for relatively weak field ($\beta_0 = 10^5$), MRI dynamo leads to repeated flips of large-scale toroidal field, with very irregular cycles. Dynamo activities tends to be suppressed for stronger fields ($\beta_0 = 10^4$). Our simulations also show secular behavior on the evolution of mean toroidal field, especially in simulations at 30 AU. This is to a certain extent related to the limitations of shearing-box, since the net vertical magnetic flux ought to be connected to infinity but gets truncated by the vertical boundary condition without reaching all the critical points (e.g., Fromang et al. 2013).

We also find that most of our simulations show strong concentration of vertical magnetic flux into a thin azimuthal shell at certain radial location, while the rest of the regions have close to zero net vertical flux. The concentration is generally stronger in simulations with stronger net vertical field ($\beta_0 = 10^4$) and toward outer disk radii ($\gtrsim 15$ AU). The concentration differs from the zonal field due to the Hall effect (Kunz & Lesur 2013), but appears to be generic in shearing-box simulations with net vertical magnetic flux and turbulence. Accompanied with magnetic flux concentration is enhanced density variation across the radial domain, with most flux is concentrated in low density regions. While this is likely the origin of enhanced zonal flow from shearing-box simulations (Simon & Armitage 2014), it remains to clarify the physics of magnetic flux concentration, and study its saturation amplitude in global context.

While all our simulations launch disk outflows, it is uncertain whether such outflows (at $\gtrsim 15$ AU) can be incorporated into a global magnetocentrifugal wind due to MRI dynamo and symmetry issues (Bai & Stone 2013a), but if they do, the level of net vertical flux $\beta_0 = 10^5$ and stronger are generally sufficient to drive accretion at desired level of $10^{-8} M_\odot \text{ yr}^{-1}$. On the other hand, to rely on purely radial transport of angular momentum by Maxwell and Reynolds stresses, the level of net vertical field must be $\beta_0 = 10^4$ or stronger assuming MMSN disk model. This level of field translates to physical field strength according to

$$B = 18.6\beta^{-1/2}R_{\text{AU}}^{-13/8} \text{ G} . \quad (14)$$

For reference, we find for $\beta_0 = 10^4$, $B_{z0} \sim 0.7$ mG at 30 AU.

7.2. Discussions

Combining the results from this paper and paper I together, we see that the Hall effect has major influence to the disk dynamics toward inner region of PPDs ($\lesssim 15$ AU) where polarity dependence is most prominent in determining the wind properties, stability to the MRI, and the amplification/reduction of horizontal magnetic field in the Hall dominated regions. The Hall effect also affect the stability to the MRI in the midplane region of the

outer disk though it is not quite significant in setting the level of turbulent motions. Overall, it is likely that wind-driven accretion dominates the inner disk while accretion can be largely driven by the MRI at surface FUV layer in the outer disk, as outlined in the discussion of Bai (2013), which incorporated numerical simulation results without the Hall effect (Bai & Stone 2013b; Simon et al. 2013a). On the other hand, detailed behavior in the inner disk region, as well as the transition from the largely laminar inner region to the MRI turbulent outer disk region, are expected to have strong polarity dependence due to the Hall effect, as summarized in the previous subsection, and also in paper I and Lesur et al. (2014).

Several observational consequences are expected based on our current simulation results. First, the fact that the inner disk launches a magnetocentrifugal wind can be detectable through gas tracers. In fact, signatures of low velocity disk outflow have been routinely inferred from blue-shifted emission line profiles such as from CO, OI and NeII lines (e.g., Hartigan et al. 1995; Pascucci & Sterzik 2009; Pontoppidan et al. 2011; Herczeg et al. 2011; Sacco et al. 2012; Rigliaco et al. 2013). While conventionally interpreted as signatures of photo-evaporation (e.g., Gorti et al. 2009; Owen et al. 2010), magnetocentrifugal wind is likely to produce similar signatures, since they possess low velocities near the launching point before getting strongly accelerated and diluted. In reality, both mechanisms are likely to contribute to launching the outflow due to the combination of UV radiative transfer and photochemistry, thermodynamics, and magnetic fields. We note that a pure photo-evaporative wind is likely to be *angular-momentum* conserving since the radial driving force does not exert any torque to the outflow, while a magnetocentrifugal wind is more likely to be *angular-velocity* conserving near the base of the wind where the gas is forced to move along supra-thermal magnetic fields anchored to the disk (e.g., Spruit 1996). Searching for distinguishable signatures between the two scenarios would be important for understanding the nature of the observed disk outflows.

Second, we expect the level of turbulence in the outer disk to be layered, where the level of turbulence is expected to be of the order $\delta v_z \sim 10^{-2} c_s$ at midplane and increases to near sonic level toward disk surface (the full turbulent velocity is further higher). Empirical constraint on the level of turbulence in the outer region of PPDs has already been reported based on the turbulent line width of the CO (3-2) transition (Hughes et al. 2011). This line is optically thick and probes the disk surface layer with line width constrained to be $\lesssim 10 - 40\%$ of sound speed, consistent with a fully turbulent surface layer. With superb sensitivity and resolution, ALMA is expected to constrain the variations of turbulence level at different disk heights using different line tracers, which will provide direct evidence of layered structure of the outer PPDs.

Third, the weakly turbulent outer disk with toroidal dominated field configuration may lead to grain alignment and dust polarization (Cho & Lazarian 2007). We have found that in the outer disk ($\gtrsim 30$ AU), the net vertical field needs to be $\beta_0 \sim 10^4$ or stronger for Maxwell stress to drive accretion rate of $10^{-8} M_\odot \text{ yr}^{-1}$. For such level of net vertical field, we see that the MRI dy-

namo is suppressed, and the entire field is dominated by a large-scale toroidal magnetic field, whose strength at disk midplane corresponds to plasma $\beta \sim 10 - 20$ (e.g., see Figure 13). Using Equation (14), we find the midplane toroidal field can be at least $\sim 3 - 8$ mG at 60 - 100 AU. Based on Equation (1) of Hughes et al. (2009), and using the MMSN disk model at midplane with grain size of 10 - 100 μm and dust aspect ratio $s = 3$, we find the critical strength for grain alignment to occur is $\sim 1 - 40$ mG at 60-100 AU. While there are large theoretical uncertainties, we see that the match is marginal, and the field strength in the outer disk can either be just enough for promoting grain alignment, or a little too weak to align the grains. Several observational attempts to search for dust polarization in Class II disks have failed (Hughes et al. 2009, 2013). Very recently, however, successful detection of dust polarization toward younger sources have been reported, with inferred field configuration resembling large scale toroidal field (Rao et al. 2014, Stephens et al., in preparation). This might indicate that disk magnetic field fades over time. Again, future dust polarization observations by ALMA will likely provide better constraints on the geometry, strength and evolution of disk magnetic fields.

From this work together with paper I, we have explored the main parameter space on the gas dynamics of PPDs using local shearing-box simulations. There are other unexplored parameters and uncertainties including the abundance and size distribution of grains, where tiny grains such as polycyclic-aromatic-hydrocarbons may reduce the importance of the Hall effect and AD hence promote the MRI (Bai 2011b). Also, the cosmic-ray ionization rate may be reduced and modulated by stellar wind/disk wind (Cleeves et al. 2013), the X-ray luminosity can be highly variable due to stellar flares (Wolk et al. 2005; Ilgner & Nelson 2006), and FUV photons may be shielded by the dust in the disk wind from the inner disk (Bans & Königl 2012). It is likely that grain abundance and FUV ionization are more sensitive parameters (Bai & Stone 2013b; Simon et al. 2013a, paper I), and X-ray ionization is less sensitive but also important (Bai

2011a, paper I).

Probably the largest uncertainties in our work come from the use of local shearing-box framework, and there are several outstanding issues resulting from the net vertical magnetic flux. With net vertical flux, it has been well known that the properties of the disk outflow is not well characterized in shearing-box simulations largely because the vertical gravitational potential is ever-increasing in the local approximation (Fromang et al. 2013; Bai & Stone 2013b). The issues related to the symmetry and fate of the outflow is notorious (Bai & Stone 2013a,b). Moreover, the evolution of large-scale magnetic field can be affected by the vertical outflow boundary condition. In this paper, we further identify the issue with the concentration of vertical magnetic flux into thin shells which resides in low-density regions in the zonal flow. Global disk simulations with vertical stratification and net vertical magnetic flux have recently been carried out (Suzuki & Inutsuka 2014), yet many of these issues remain not quite addressed due to limited domain size in the θ dimension. In the future, it is crucial to perform global simulations with sufficiently large vertical domain to accommodate the disk outflow/wind, and fine resolution in the disk to resolve the disk microphysics. In this way, these critical issues can potentially and ultimately be appropriately addressed.

I thank Jim Stone for helpful discussions and useful comments to the draft. This work is supported from program number HST-HF-51301.01-A provided by NASA through a Hubble Fellowship grant from the Space Telescope Science Institute awarded to XN.B, which is operated by the Association of Universities for Research in Astronomy, Incorporated, under NASA contract NAS5-26555. Computation for this work was performed on Stampede at Texas Advanced Computing Center through XSEDE grant TG-AST140001, and on Kraken at National Institute for Computational Sciences through XSEDE grant TG-AST130048.

REFERENCES

- Bai, X.-N. 2011a, *ApJ*, 739, 50
 —. 2011b, *ApJ*, 739, 51
 —. 2013, *ApJ*, 772, 96
 —. 2014, *ApJ*, submitted, arXiv:1402.7102 (paper I)
 Bai, X.-N. & Goodman, J. 2009, *ApJ*, 701, 737
 Bai, X.-N. & Stone, J. M. 2011, *ApJ*, 736, 144
 —. 2013a, *ApJ*, 767, 30
 —. 2013b, *ApJ*, 769, 76
 Balbus, S. A. & Hawley, J. F. 1991, *ApJ*, 376, 214
 Balbus, S. A. & Terquem, C. 2001, *ApJ*, 552, 235
 Bans, A. & Königl, A. 2012, *ApJ*, 758, 100
 Chapman, N. L., Davidson, J. A., Goldsmith, P. F., Houde, M., Kwon, W., Li, Z.-Y., Looney, L. W., Matthews, B., Matthews, T. G., Novak, G., Peng, R., Vaillancourt, J. E., & Volgenau, N. H. 2013, *ApJ*, 770, 151
 Cho, J. & Lazarian, A. 2007, *ApJ*, 669, 1085
 Cleeves, L. I., Adams, F. C., & Bergin, E. A. 2013, *ApJ*, 772, 5
 Crutcher, R. M. 2012, *ARA&A*, 50, 29
 Davis, S. W., Stone, J. M., & Pessah, M. E. 2010, *ApJ*, 713, 52
 Desch, S. J. 2004, *ApJ*, 608, 509
 Fleming, T. & Stone, J. M. 2003, *ApJ*, 585, 908
 Fromang, S., Latter, H., Lesur, G., & Ogilvie, G. I. 2013, *A&A*, 552, A71
 Goldreich, P. & Lynden-Bell, D. 1965, *MNRAS*, 130, 125
 Gorti, U., Dullemond, C. P., & Hollenbach, D. 2009, *ApJ*, 705, 1237
 Hartigan, P., Edwards, S., & Ghandour, L. 1995, *ApJ*, 452, 736
 Hawley, J. F., Guan, X., & Krolik, J. H. 2011, *ApJ*, 738, 84
 Hayashi, C. 1981, *Progress of Theoretical Physics Supplement*, 70, 35
 Herczeg, G. J., Brown, J. M., van Dishoeck, E. F., & Pontoppidan, K. M. 2011, *A&A*, 533, A112
 Hughes, A. M., Hull, C. L. H., Wilner, D. J., & Plambeck, R. L. 2013, *AJ*, 145, 115
 Hughes, A. M., Wilner, D. J., Andrews, S. M., Qi, C., & Hogerheijde, M. R. 2011, *ApJ*, 727, 85
 Hughes, A. M., Wilner, D. J., Cho, J., Marrone, D. P., Lazarian, A., Andrews, S. M., & Rao, R. 2009, *ApJ*, 704, 1204
 Hull, C. L. H., Plambeck, R. L., Kwon, W., Bower, G. C., Carpenter, J. M., Crutcher, R. M., Fiege, J. D., Franzmann, E., Hakobian, N. S., Heiles, C., Houde, M., Hughes, A. M., Lamb, J. W., Looney, L. W., Marrone, D. P., Matthews, B. C., Pillai, T., Pound, M. W., Rahman, N., Sandell, G., Stephens, I. W., Tobin, J. J., Vaillancourt, J. E., Volgenau, N. H., & Wright, M. C. H. 2014, *ApJ*, submitted
 Ilgner, M. & Nelson, R. P. 2006, *A&A*, 455, 731
 Johansen, A., Youdin, A., & Mac Low, M. 2009, *ApJ*, 704, L75
 Kunz, M. W. 2008, *MNRAS*, 385, 1494

- Kunz, M. W. & Balbus, S. A. 2004, *MNRAS*, 348, 355
- Kunz, M. W. & Lesur, G. 2013, *MNRAS*, 434, 2295
- Lesur, G., Kunz, M. W., & Fromang, S. 2014, *ArXiv e-prints*
- McElroy, D., Walsh, C., Markwick, A. J., Cordiner, M. A., Smith, K., & Millar, T. J. 2013, *A&A*, arXiv:1212.6362
- McKee, C. F. & Ostriker, E. C. 2007, *ARA&A*, 45, 565
- Oishi, J. S. & Mac Low, M. 2009, *ApJ*, 704, 1239
- Oppenheimer, M. & Dalgarno, A. 1974, *ApJ*, 192, 29
- Owen, J. E., Ercolano, B., Clarke, C. J., & Alexander, R. D. 2010, *MNRAS*, 401, 1415
- Pandey, B. P. & Wardle, M. 2012, *MNRAS*, 3001
- Pascucci, I. & Sterzik, M. 2009, *ApJ*, 702, 724
- Perez-Becker, D. & Chiang, E. 2011, *ApJ*, 735, 8
- Pontoppidan, K. M., Blake, G. A., & Smette, A. 2011, *ApJ*, 733, 84
- Rao, R., Girart, J. M., Lai, S.-P., & Marrone, D. P. 2014, *ApJ*, 780, L6
- Rigliaco, E., Pascucci, I., Gorti, U., Edwards, S., & Hollenbach, D. 2013, *ApJ*, 772, 60
- Sacco, G. G., Flaccomio, E., Pascucci, I., Lahuis, F., Ercolano, B., Kastner, J. H., Micela, G., Stelzer, B., & Sterzik, M. 2012, *ApJ*, 747, 142
- Sano, T. & Stone, J. M. 2002a, *ApJ*, 570, 314
- . 2002b, *ApJ*, 577, 534
- Shi, J., Krolik, J. H., & Hirose, S. 2010, *ApJ*, 708, 1716
- Simon, J. B. & Armitage, P. J. 2014, *ApJ*, 784, 15
- Simon, J. B., Bai, X.-N., Armitage, P. J., Stone, J. M., & Beckwith, K. 2013a, *ApJ*, 775, 73
- Simon, J. B., Bai, X.-N., Stone, J. M., Armitage, P. J., & Beckwith, K. 2013b, *ApJ*, 764, 66
- Sorathia, K. A., Reynolds, C. S., Stone, J. M., & Beckwith, K. 2012, *ApJ*, 749, 189
- Spruit, H. C. 1996, in *NATO ASIC Proc. 477: Evolutionary Processes in Binary Stars*, ed. R. A. M. J. Wijers, M. B. Davies, & C. A. Tout, 249–286
- Stone, J. M., Gardiner, T. A., Teuben, P., Hawley, J. F., & Simon, J. B. 2008, *ApJS*, 178, 137
- Suzuki, T. K. & Inutsuka, S.-i. 2009, *ApJ*, 691, L49
- . 2014, *ApJ*, 784, 121
- Walsh, C., Millar, T. J., & Nomura, H. 2010, *ApJ*, 722, 1607
- Walsh, C., Nomura, H., Millar, T. J., & Aikawa, Y. 2012, *ApJ*, 747, 114
- Wardle, M. 1999, *MNRAS*, 307, 849
- . 2007, *Ap&SS*, 311, 35
- Weidenschilling, S. J. 1977, *MNRAS*, 180, 57
- Wolk, S. J., Harnden, Jr., F. R., Flaccomio, E., Micela, G., Favata, F., Shang, H., & Feigelson, E. D. 2005, *ApJS*, 160, 423